




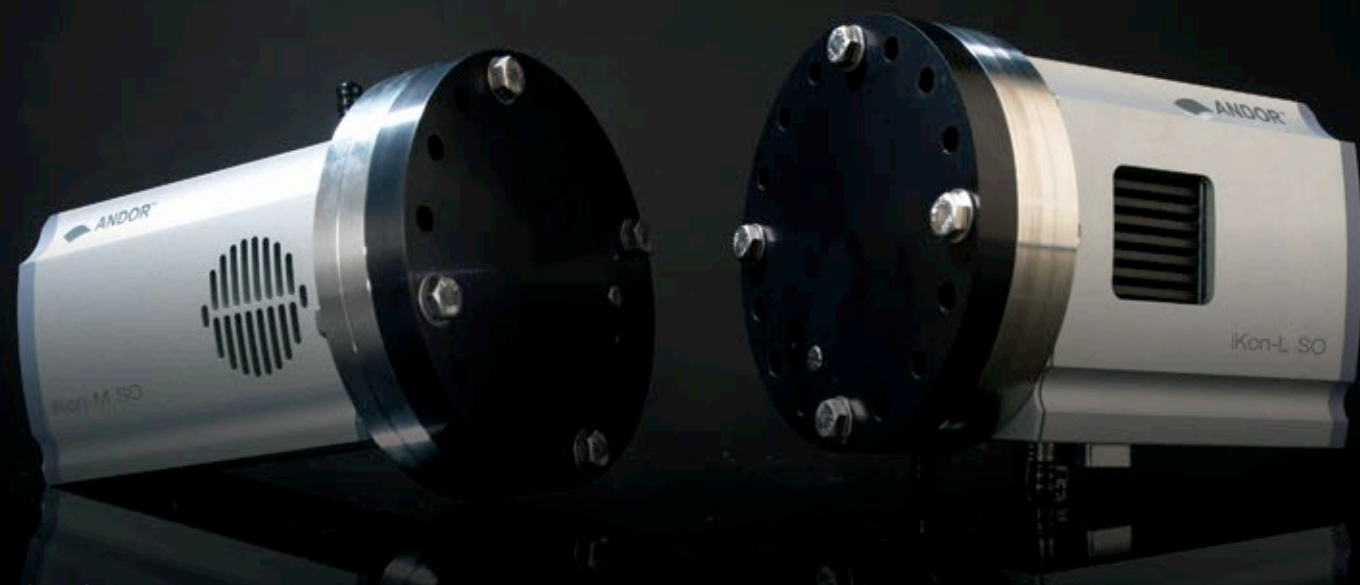
High Energy Detection

Solutions Beyond The Visible



Contents

- 03 Overview
- 04 Detection Beyond The Visible
- 06 High Energy Detection
- 09 The Interfaces
 - 10  - 'Open Front'
 - 11  - 'Fiber-Optic'
 - 12  - 'Stand Alone'
- 13 The Camera Platforms
 - 14 Extending Andor's 'Standard' Cameras For High Energy Detection
 - 15 Standard Ultra Sensitive Cameras For Lens Coupled Indirect Detection
- 16 Focus On High Energy Spectroscopy
- 19 Customer Special Request (CSR)
- 20 High Energy Camera Capabilities
- 22 Defining A Solution
- 24 Software Solutions
- 25 Accessories
- 26 Application and Technical Notes
- 48 Standard Part Numbers
- 50 Research Papers
- 53 Looking After Your System



Overview

Benefiting from over 20 years of cutting edge development and manufacture, Andor's comprehensive range of high energy camera detection systems addresses a wide variety of imaging and spectroscopy applications from cell structure studies and medical research to material analysis.

These 'direct' or 'indirect' detection systems can be used at varying energy levels and are configured to operate across a number of sampling interfaces. For example, can interface with a vacuum chamber via a mounting flange. Fiber-optic coupled configurations are also available to interface with external scintillators or imaging relays such as streak tubes.

Andor's high energy detection platforms are built to last and are engineered from the outset with ease of use in mind; every system is developed to integrate quickly and directly into the heart of the experimental setup.

Andor also offers expertise in bespoke customization to arrive at novel detection solutions to your specific experimental requirements.

“ Using the Andor DO420-BN CCD camera, we could observe the radial profile of impurity line emission from LHD fusion plasmas in EUV range to study the impurity transport. This was the first time in magnetic confinement fusion research that the radial profile was observed in EUV range with such good results.



Prof. Shigeru Morita, National Institute for Fusion Science, Japan

”



Detection Beyond The Visible

Andor's high energy camera solutions cover a broad wavelength range, spanning VUV, EUV, X-Ray and gamma regions. Detection is achieved either through direct detection of the high energy photon by the sensor or by indirect detection of visible photons emitted from a phosphor or scintillator, either a fiber-optic or a lens coupled to the detector.

| Region | Energy [keV] | Typical Application |
|-------------------------|--------------|---|
| VUV to XUV [EUV] | 0.01 - 0.1 | EUV Lithography |
| [EUV] XUV to Soft X-Ray | 0.1 - 1 | Soft X-Ray Imaging / Microscopy |
| Soft to Hard X-Ray | 1 - 14 | X-Ray Spectroscopy (e.g. SAXA), Plasma Diagnostics |
| Hard X-Ray | 14 - 100 | Diffraction / Crystallography, Phase Contrast Imaging |
| Hard X-Ray to Gamma | 100+ | Gamma Tomography |

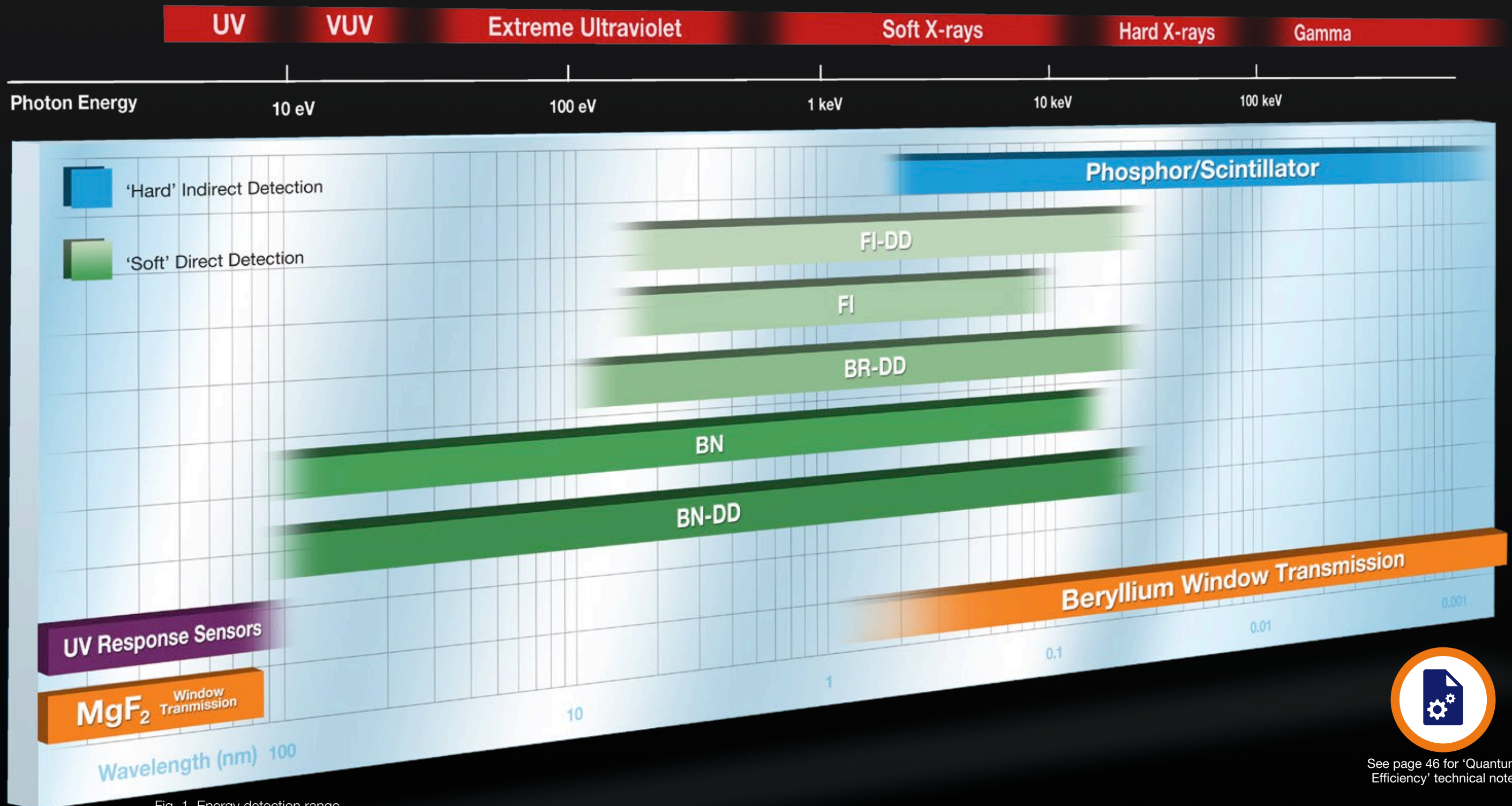


Fig. 1. Energy detection range



See page 46 for 'Quantum Efficiency' technical note

High Energy Detection

The two main methods of detecting high energy photons with scientific cameras are 'Direct' and 'Indirect' detection.

Direct Detection

Andor employs the notation 'S' to indicate cameras that are optimal for detection of 'soft' lower energy photons.

With direct detection, the incident VUV to soft X-Ray photon is absorbed directly within the silicon of the sensor resulting in the production of multiple electron-hole pairs. This method of detection limits the range of usage of the sensor to photon energies that silicon can absorb directly, as shown in Fig. 1 on page 4.

The design and architecture of the sensor and camera directly affect the detection range. Therefore an uncoated back-illuminated sensor will allow low energy photons to pass into the depletion zone to be absorbed, while a deep-depletion device allows higher energy photons to be absorbed by the increased depth of active silicon.

Advantages

- Good spatial resolution
- Single photon sensitivity
- Energy resolution
- Good QE
- Linear response
- High dynamic range

Limitations

- Cannot detect hard X-Rays > 20 keV
- Upper limit on image area (typically ~ 25 x 25 mm)
- CCD 'degrades' progressively under energetic X-Ray radiation exposure

Typical 'S' Applications

- EUV lithography
- Soft X-Ray imaging / microscopy
- X-Ray spectroscopy
- Plasma diagnostics
- X-Ray lithography
- X-Ray diffraction
- X-Ray Photon Correlation Spectroscopy (XPCS)
- Small-Angle X-Ray Scattering (SAXS)



See page 46 for 'Quantum Efficiency' technical note



See page 48 for 'Direct Detection' technical note

Indirect Detection

Andor employs the notation 'H' to indicate cameras that are optimal for detection of 'hard' higher energy photons.

Indirect detection employs a material, such as a scintillator or phosphor, to convert incident high energy X-Ray or gamma photons to photons of visible wavelength, which can then be detected directly by the sensor.

A fiber-optic can be used to couple the scintillator to the camera. This can bear several advantages including protection of the sensor from damage by the higher energy photons, improving the camera's spatial resolution and, with tapers, providing the ability to extend the detection field of view beyond that defined by the sensor active area.

Advantages

- Higher dynamic range
- EMCCD compatible – single photon sensitivity
- Large area magnifying tapers
- Wide photon energy coverage into the hard X-Ray and gamma range
- High frame rate

Limitations

- Lower spatial resolution
- Lower energy resolution

Typical 'H' Applications

- Microtomography
- X-Ray diffraction
- X-Ray crystallography
- X-Ray medical imaging
- Industrial inspection
- Streak tube readout



See page 47 for 'Indirect Detection' technical note




The Interfaces

Andor has a comprehensive portfolio of imaging and spectroscopic camera platforms developed for use in a wide range of high energy applications. To suit these many different requirements it is often necessary to modify the camera's interface to allow optimal integration with the sampling environment.

This section highlights Andor's dedicated range of interface types and their associated identifiers: O, Y and F. The interface identifier is then combined with either the 'S' or 'H' identifier. Together these then fully define both the energy range and sampling environment that the camera solution is suited to.

“ The large area X-Ray Andor CCD system has been used to acquire much more data on each shot, enabling researchers using the Central Laser Facilities to make significantly faster progress than previously possible.



Prof. David Neely, Central Laser Facility, Harwell Science and Innovation Campus, Oxfordshire, UK

”

| Interface | Description | Direct  | Indirect  |
|---|--------------------------------------|--|--|
|  | Open faced coupled to vacuum chamber | SO | HO |
|  | Stand alone - beryllium window | SY | HY |
|  | Multi-MHz readout with fiber-optic | - | HF |

Phase-Contrast Tomography of Armadillidiidae (Pill Bug/Roly Poly)

by Will Schumaker of the Center for Ultrafast Optical Science, University of Michigan, USA

O Interface - 'Open Front' design

Andor's 'O' interface type describes an open front design, coupling directly onto a vacuum chamber's port, ensuring maximum detection efficiency and spatial resolution.

'Open front' cameras are designed to be coupled to the outside of a vacuum chamber. There are two types of sealing options available: knife edge and O-ring seal.

The design allows use of a removable filter holder, and the system interface allows the camera to be cooled either by air or water.

Mounting flange options can be supplied for all standards, including rotatable where applicable.

| Features |
|---|
| Both spectroscopic and imaging formats available |
| Full range of sensor options available |
| O-ring and knife edge sealing options |
| Range of standard flange options, with custom made available on request |
| Standard cooling options available |
| Optional filter holder with a range of filter options |
| Indirect capability - phosphor coated fiber-optic or scintillators |

Two-In-One Capability

Andor's unique 'O-Y Converter' accessory can be used to modify Andor's 'Open Front' design to that of a 'Stand alone' Beryllium window design.



See page 27 for Andor's O-Y converter accessory

F Interface - 'Fiber-Optic' design

A number of Andor's camera platforms can be configured with the 'F' type protruding fiber-optic interface, ideal for indirect detection of high energy X-Ray or gamma photons that are incident on a phosphor or scintillator.

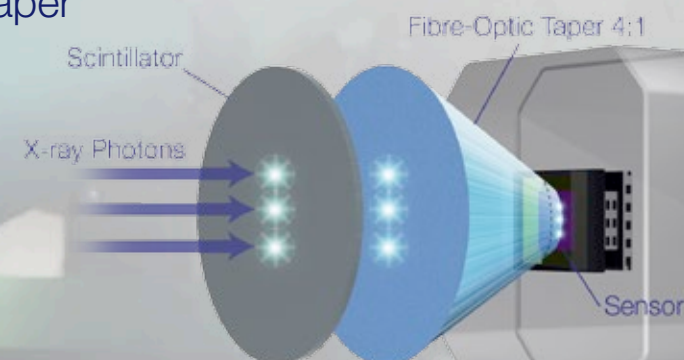
A fiber-optic interface can be coupled to either front-illuminated or back-illuminate sensors. A range of phosphor and scintillator options are available, specifically selected to match your required energy range.

The fiber-optic interface is available not just for CCD detectors (e.g. the iKon platform), but also on Electron Multiplying CCD (EMCCD) and scientific CMOS (sCMOS) sensor technology, via Andor's high performance iXon and Zyla camera platforms respectively.

Andor's back-illuminated iXon offers single photon sensitivity at fast frame rates. The higher sensitivity of the iXon EMCCD cameras is particularly relevant where photon loss through a fiber-optic taper is involved.

| Features |
|---|
| Fiber-optic bonding optimized to deliver highest throughput and resolution |
| Optimal phosphors / scintillators for specific energies available on request |
| Available with 1:1 fiber optic or tapered option for larger field-of-view capture |
| EMCCD options where speed and low flux are key parameters |
| Fiber bonding to front or back-illuminated sensors |
| sCMOS options where faster speed is a key parameter |
| Flanges designed to allow direct coupling to scintillator |

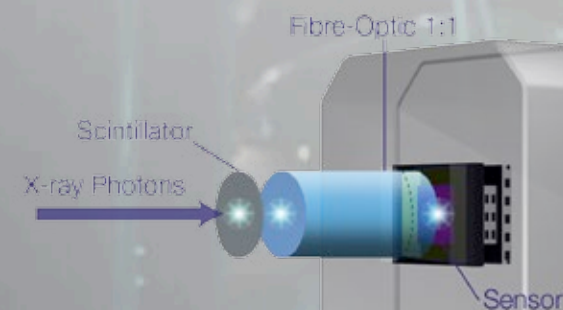
Taper



Unique Fiber-Optic EMCCD Capability

Andor's fiber-coupled iXon EMCCD detector provides single photon sensitivity at rapid frame rates, ideal for tomographic applications and to counter high photon loss through tapers.

1:1



NEW - Zyla sCMOS

Andor's Zyla sCMOS detector provides even faster frame rates with higher field of view, allowing faster capture and processing of large tomographic data sets, or study of fast transient phenomena.

Y Interface - 'Stand Alone' design

Andor's 'Y' style interface is available across the iKon and Newton CCD camera platforms, and is built with a window that blocks visible wavelengths but allows higher energy photons through to the sensor. It is ideal for direct detection in the soft X-Ray energy range or, with inclusion of a phosphor coated fiber-optic, for indirect detection of hard X-Ray photons.

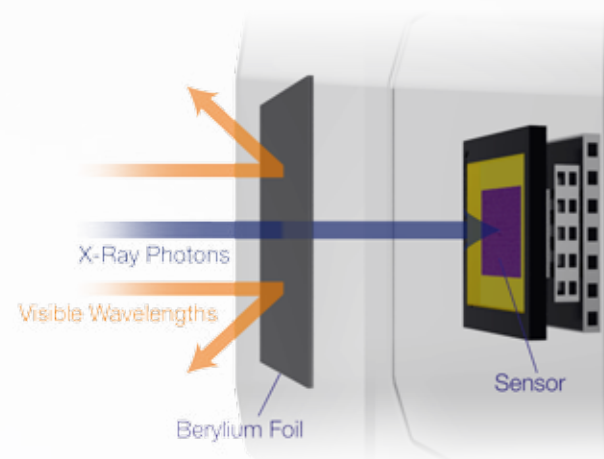
The 'Stand Alone' design indicates that it is constructed to operate outside a vacuum chamber. The standard window used is made from Beryllium although other materials can be used, for example Aluminium.

This interface type is available for both direct and indirect detection. 'Y' cameras are available for direct detection applications with a range of sensor QE options, or for indirect detection applications with a phosphor coated fiber-optic positioned over the CCD sensor.

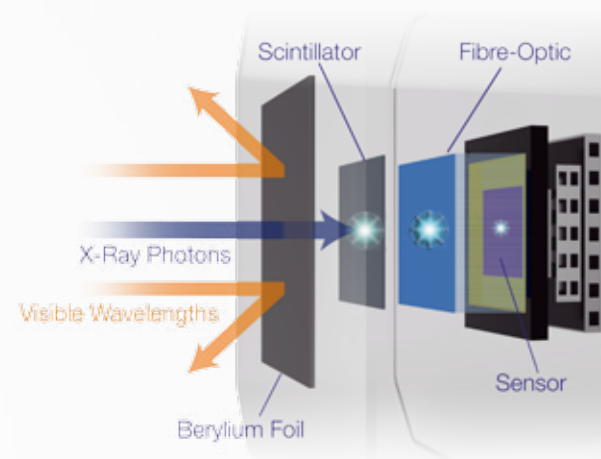
For optimal indirect detection, the energy range required will dictate the selection of phosphors or scintillators. The iKon-M and Newton 'SY' series are designed with a permanent vacuum chamber around the CCD sensor for longlasting maintenance-free operation, while an Argon backfilled enclosure is used for the iKon & Newton 'HY' and iKon L 'SY' series.

| Features |
|---|
| NEW Permanent vacuum design (iKon-M SY and Newton SY) for extended reliability |
| Both spectroscopic and imaging formats available |
| 200 µm Beryllium window as standard, with other thickness or materials available on request |
| Vacuum as standard, with other options on request |
| Indirect capability - phosphor coated fiber-optic or scintillators |

Direct 'S' Option



Indirect 'H' Option



The Camera Platforms



| | Zyla sCMOS | Newton CCD | iKon EMCCD | iKon L CCD | iKon M CCD |
|-------------------------------|---|--|--|--|---|
| Description | Compact sCMOS platform, multi megapixel array, low-noise, ultra fast frame rates and high resolution imaging. | High performance CCD camera with variable readout rates up to 3 MHz through plug and play USB interface. | This cutting edge EMCCD camera provides single photon sensitivity at fast frame rates. | Large area 4 megapixel CCD camera optimized for low noise imaging solutions, USB interface, readout rates up to 5 MHz. | 1 megapixel, low noise CCD camera for imaging solutions through a USB interface. Readout rates up to 5 MHz. |
| Model Options | Zyla 5.5 | 920P or 940P | 897 | 936 | 934 |
| Interface Options | F | O, Y | F | O, F, Y | O, F, Y |
| Pixel Size | 6.5 | 26 or 13.5 | 16 | 13.5 | 13 |
| Active Pixels | 2560 x 2160 | 1024 x 255 up to 2048 x 512 | 512 x 512 | 2048 x 2048 | 1024 x 1024 |
| Maximum full frame rate (fps) | 100 | - | 34 | 0.92 | 2.2 |
| Maximum spectra per second | - | 1612 | - | - | - |
| Sensor Area (mm) | 16.6 x 14 | Up to 26.7 x 6.9 | 8.2 x 8.2 (1:1.5 taper available) | 13.3 x 13.3 (1:1 taper) | 13.3 x 13.3 (1:1 taper) |
| PC Interface | Camera Link (10-tap) | Lockable USB 2.0 | PCI | Lockable USB 2.0 | Lockable USB 2.0 |
| Sensor Options Available | N/A | FI, BN, FI-DD, BR-DD, FO | FB | FI, BN, BR-DD, FO, BV | FI, BN, FI-DD, BR-DD, FO |

Extending Andor's 'Standard' Cameras For High Energy Detection

Extending to the 'UV'

Andor's standard range of ultra-sensitive imaging and spectroscopy camera platforms can be readily customized with a MgF₂ window, extending detection in the UV down to ~120 nm. Note, the system performance is also dependent on the QE of the sensor in the UV wavelength range.

Features

MgF₂ window allowing transmission down to 120 nm

Both spectroscopic and imaging formats available

CCD and EMCCD sensor architecture

UltraVac™ sensor enclosure / deep TE-cooling

Shielded detector cable and connections for vacuum available on request

Standard Andor sensor types that are sensitive in the UV region include:

- Lumogen coated (UVB)
- Virtual phase (VP)
- Enhanced silicon (BU2)
- Open electrode (OE)

Standard Ultra Sensitive Cameras For Lens Coupled Indirect Detection

Many applications require use of lens based cameras within indirect detection systems, where a 'stand alone' camera solution images a scintillator screen. Such applications include both X-Ray and Neutron Tomography.

The full range of Andor's ultra sensitive imaging portfolio can be considered for this approach.

Options include the iXon Electron Multiplying CCD (EMCCD) range, offering single photon sensitivity at the fast frame rates, or the ground-breaking Neo scientific CMOS (sCMOS) camera, which simultaneously offers ultra-low read noise, large field of view, high spatial resolution, wide dynamic range and extremely fast frame rates, without compromise.

Features

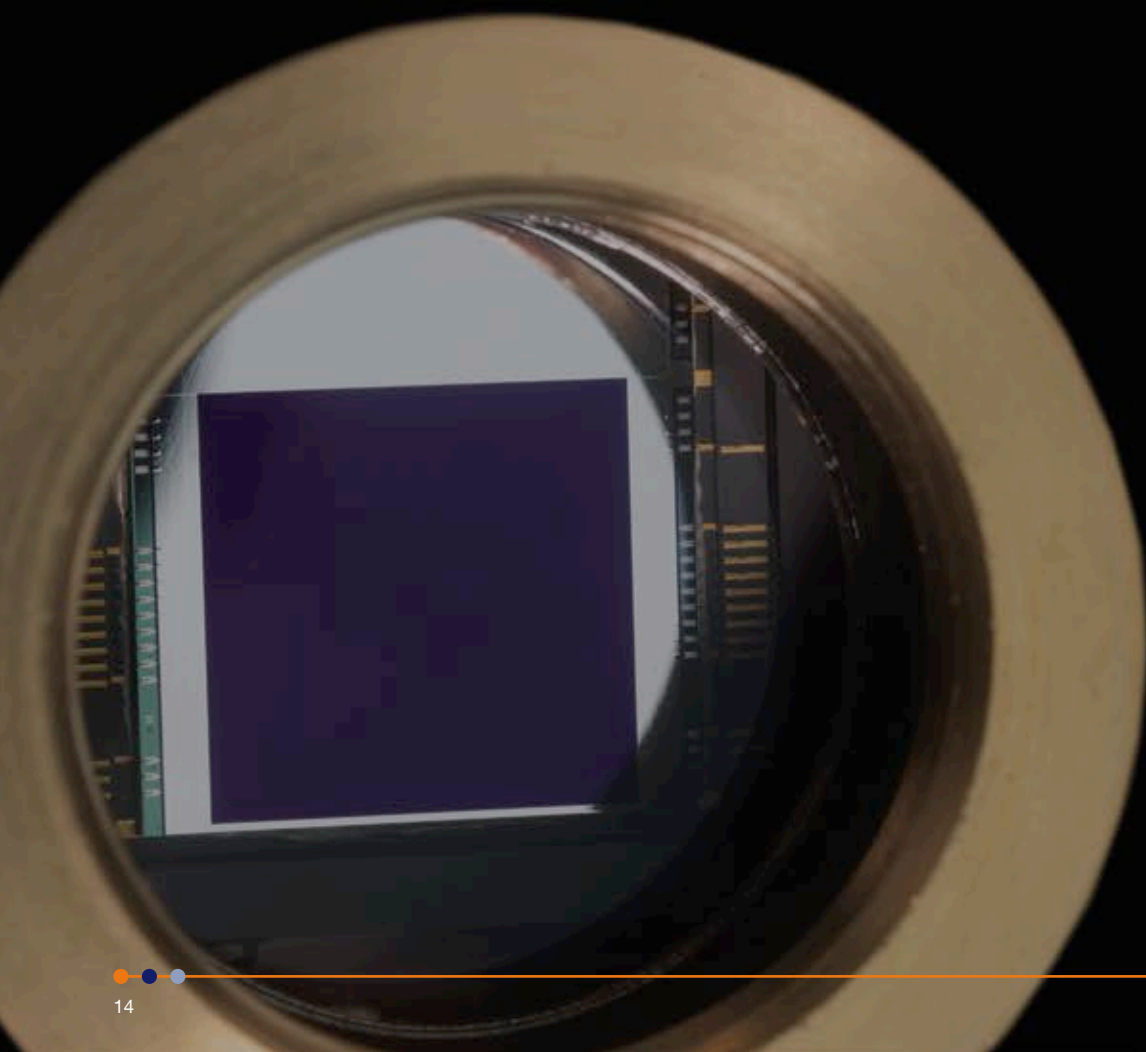
Lens coupled to scintillator - detection of 'hard' energies

Both imaging and spectroscopic formats available

CCD, EMCCD and sCMOS

UltraVac™ sensor enclosure / deep TE-cooling

Visit andor.com and click on 'Cameras' to view this market leading camera portfolio.

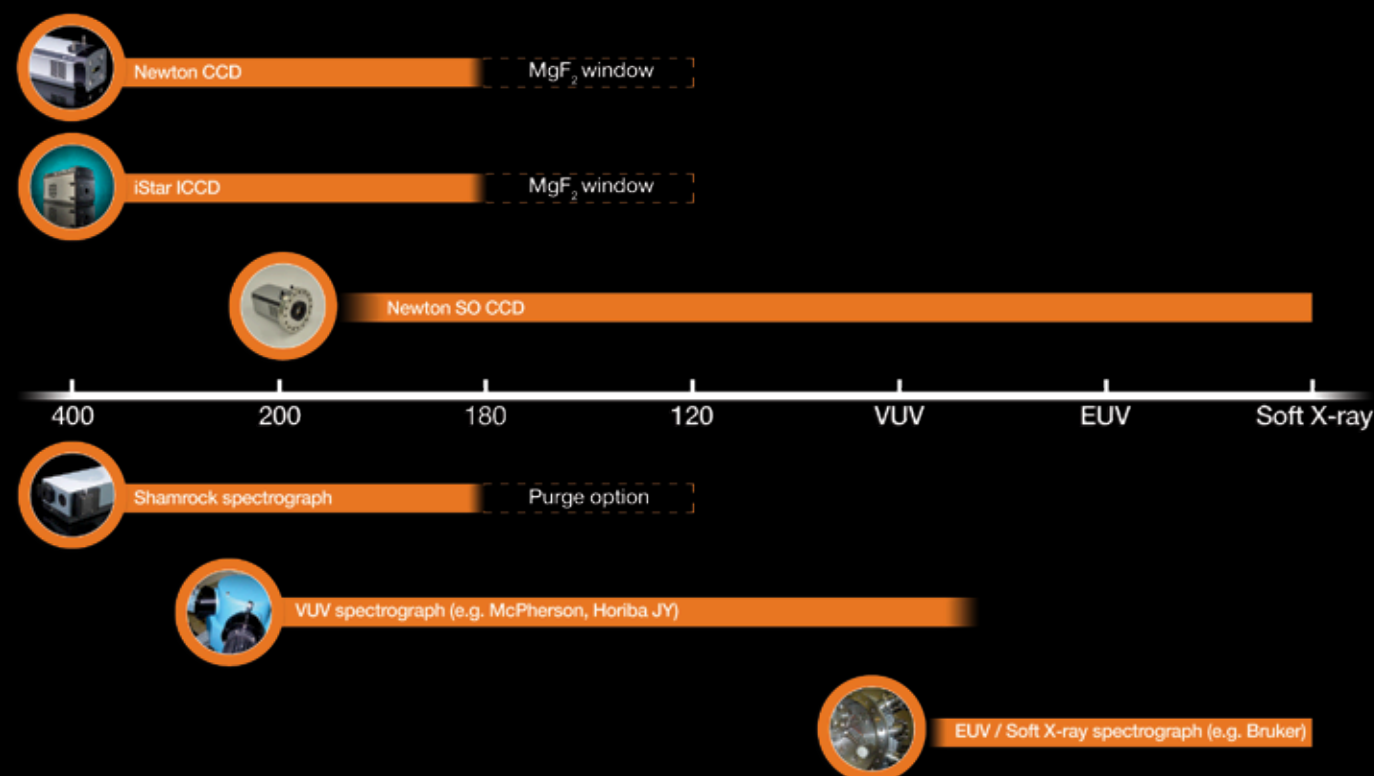


Focus On High Energy Spectroscopy

Engineered from the outset with ease-of-use and performance in mind, Andor's Spectroscopy systems feature a combination of market leading CCD, Intensified CCD detectors and UV-NIR spectral instruments.

| Typical Applications | |
|--------------------------|------------------------------|
| X-Ray Diffraction (XRD) | X-Ray plasma physics |
| X-Ray Fluorescence (XRF) | X-Ray laser characterization |
| EUV / VUV spectroscopy | HHG spectroscopy |

Andor's vacuum-compatible CCDs and Intensified CCDs combine seamlessly with market leading VUV, EUV and XUV spectral instruments to provide ultra-sensitive, ultra-fast solutions for demanding high-energy Spectroscopy setups.



See page 28 for Application and Technical notes

iStar ICCD

USB 2.0 platform, with a unique software controlled, ultra-low-jitter on-board Digital Delay Generator (DDG™) and high-voltage, high-speed gating electronics for < 2 ns time resolution down to 120 nm.

Newton CCD

The Newton series offers no compromise when it comes to high sensitivity and speed, with low-noise, multi-MHz electronics platform enabling spectral collection faster than 1600 spectra/s, ideal for transient phenomena studies.

Shamrock series

Research-grade, high performance, rugged and seamlessly configurable spectrograph platforms designed for working with demanding low-light applications in the UV – NIR range, but equally suited to routine measurements.



Customer Special Request (CSR)

At Andor we realise that, sometimes, even our adaptable and flexible off-the-shelf products are not enough to meet some of the more demanding application requirements of our customers.

For this reason we provide a bespoke service to our customers, whereby a dedicated highly experienced team of engineers and application specialists provide customer specific solutions. The process involves discussing your core requirements, advising on possible solutions, design development, quotation and final delivery of the product.



The CSR service is at the heart of the Andor ethos of offering high performance, high quality products and solution developments for each and every customer.

Our extensive capabilities, married to our flexible and adaptable approach, is very complementary to the specific needs that often arise in the sphere of the X-Ray and high energy detection community.

CSR Solutions

A CSR solution can encompass a complete system, a single camera or an accessory. Here are some examples of Andor's CSR capabilities.



- 1. Vacuum compatible adjustable tilt sensor mount
- 2. Protruding sensor on a vacuum compatible iKon-L
- 3. Pillar mounted protruding sensor on an iKon-M SO
- 4. Double sensor package in a single camera body
- 5. Beam stop
- 6. Open MCP
- 7. Camera faceplate with an ultra thin Beryllium foil beam window

High Energy Camera Capabilities

The following diagram can be used as a guide to Andor's broad capabilities in the area of high energy photon detection, demonstrating our ability to adapt our various high-performance camera platforms to meet a broad gamut of specific application and set-up requirements.

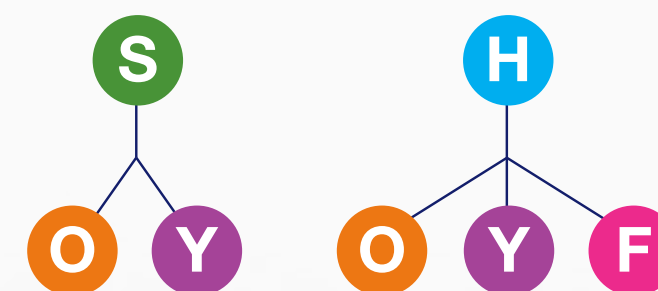
Many of the camera types represented are available as standard products, as represented on page 50 of this brochure. Please use Andor's Customer Special Request (CSR) service to discuss other options within this diagram.

- S Direct Detection Cameras
- O Open Front Systems
- H Indirect Detection Cameras
- Y Stand Alone Systems
- F Fiber Optic Interface

Zyla sCMOS NEW



iKon-M CCD



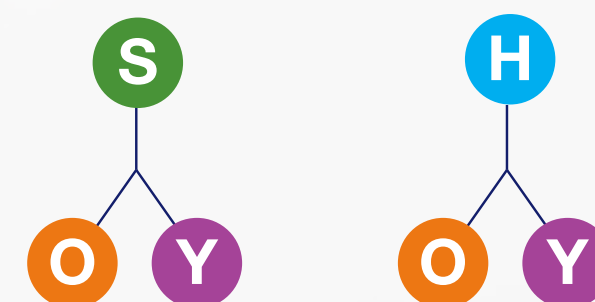
iStar ICCD



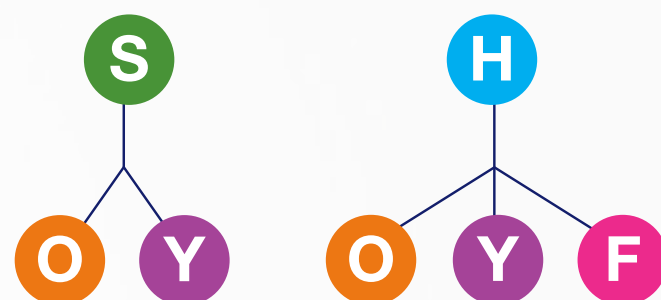
iXon EMCCD



Newton CCD

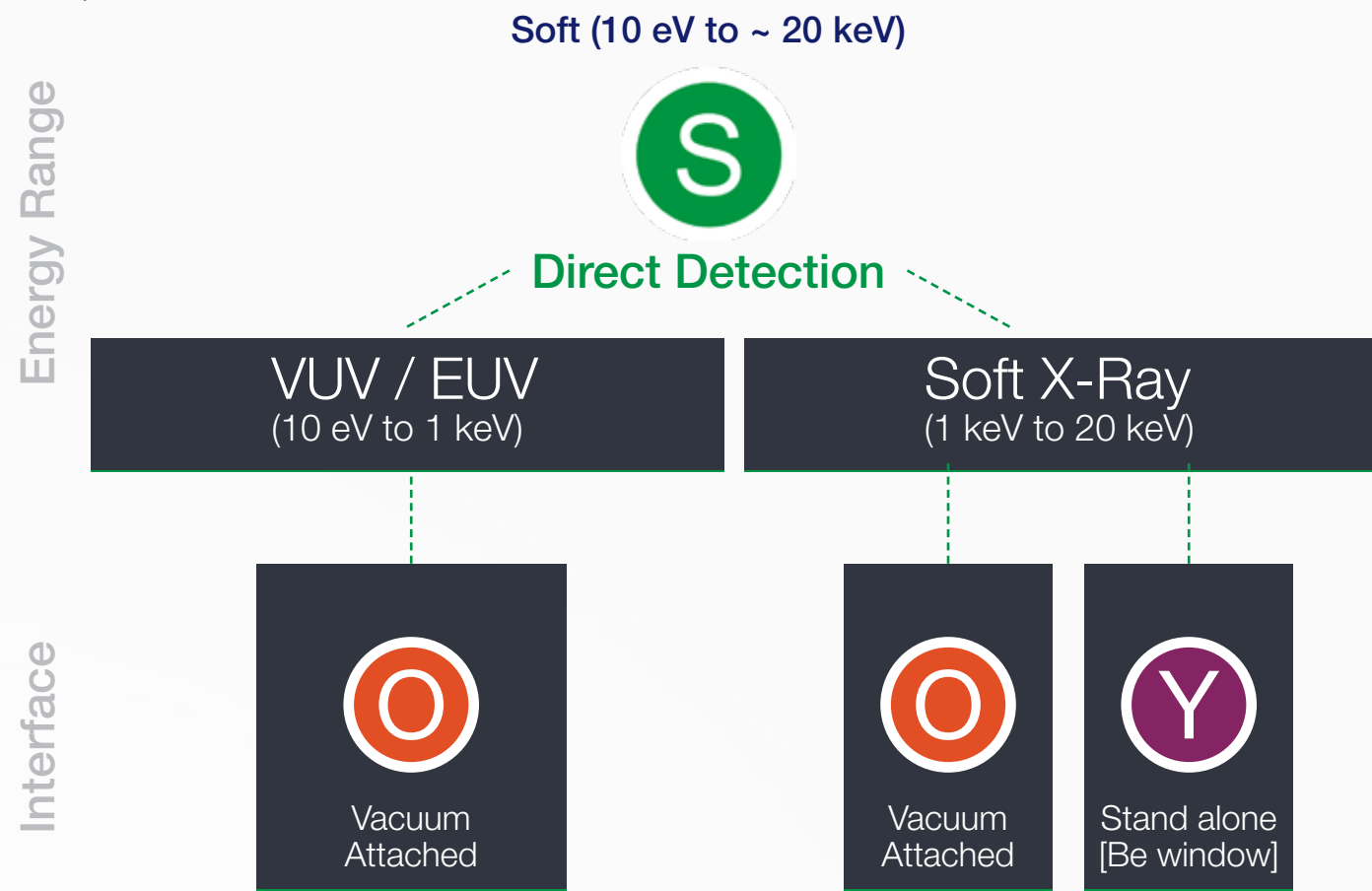


iKon-L CCD



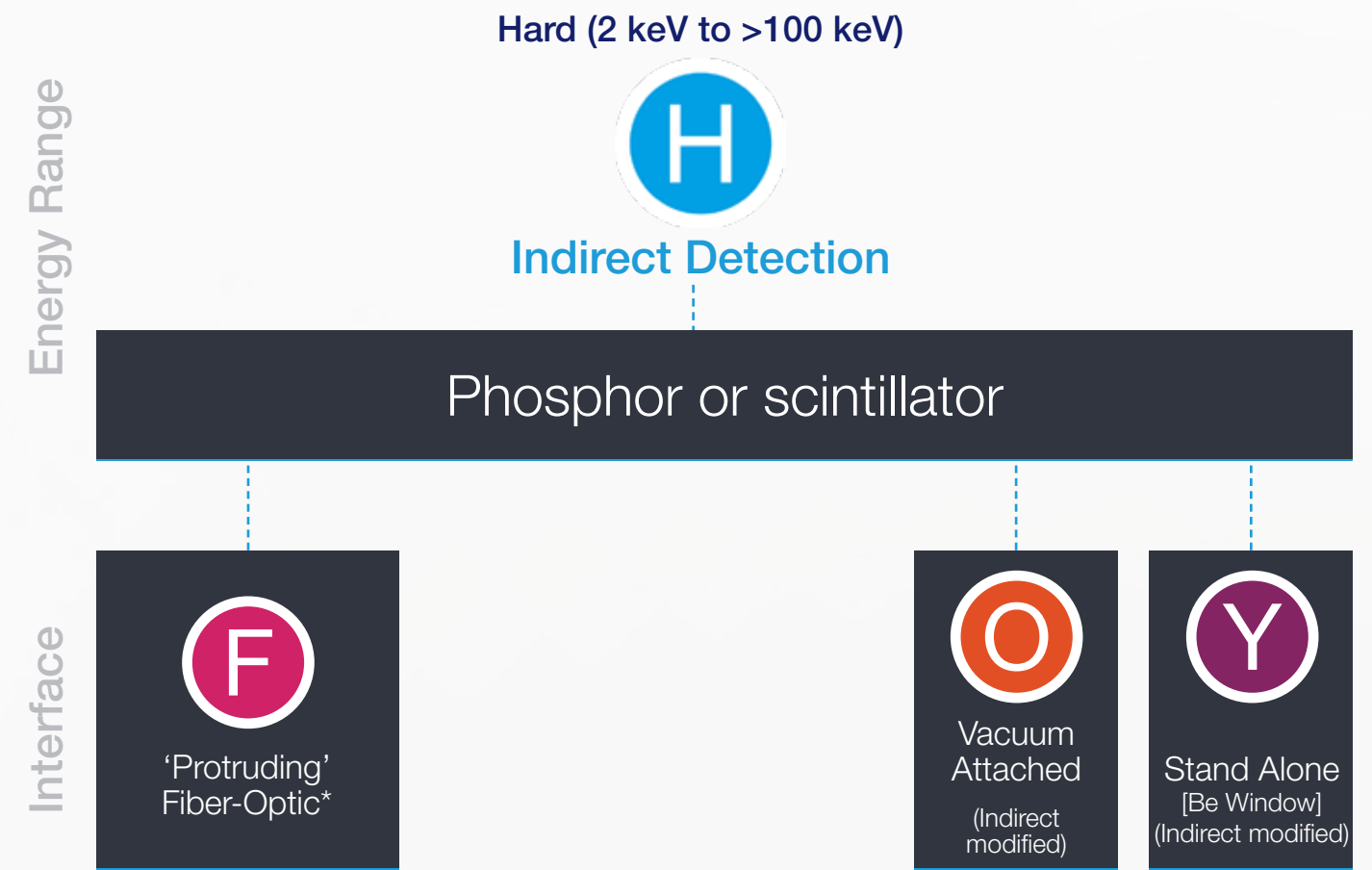
Defining A Solution

Building the optimal solution to your high energy detection requirements involves many decisions, including energy range, the 'interface' to the sampling environment, as well as attributes of the camera platform. Camera parameters include field of view, pixel size, frame rate, relative sensitivity, well depth, etc. Here we provide a high level guide to the decision steps involved.

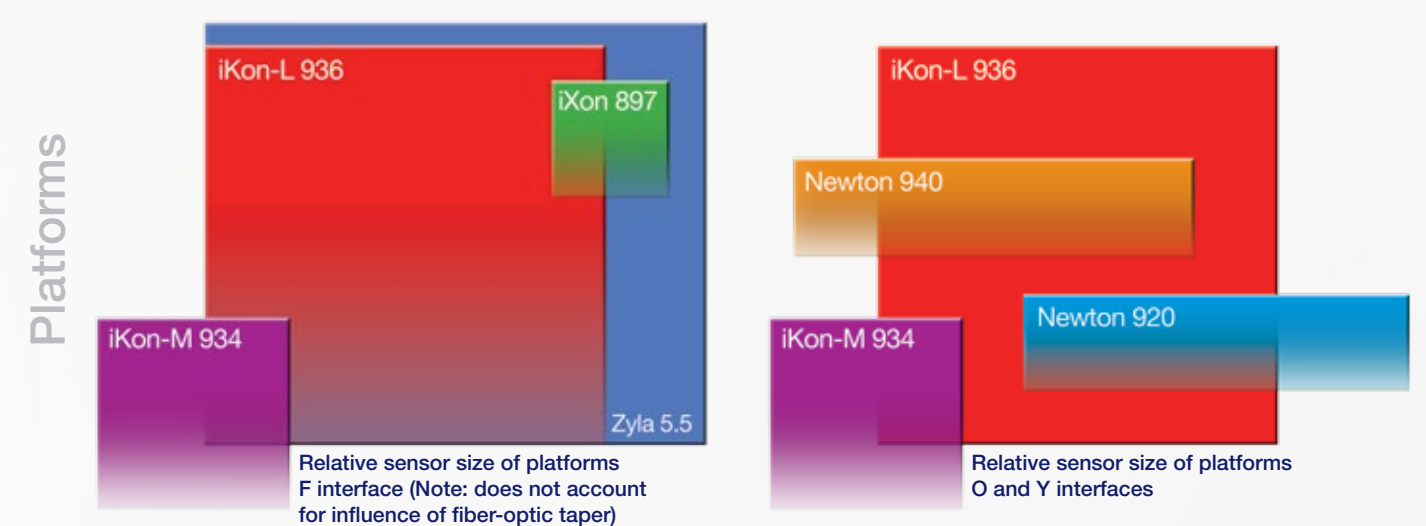


| Product | Array Size | Pixel Size (µm) | FoV (mm) |
|------------|-------------|-----------------|-------------|
| iXon 897 | 512 x 512 | 16 | 8.2 x 8.2 |
| iKon-L 936 | 2048 x 2048 | 13.5 | 27.7 x 27.7 |
| Newton 940 | 2048 x 512 | 13.5 | 27.7 x 6.9 |
| iKon-M 934 | 1024 x 1024 | 13 | 13.3 x 13.3 |
| Newton 920 | 1024 x 256 | 26 | 26.7 x 6.7 |

Sensor types available for Andor's 'S' and 'H' detection solutions.



* Practical field of view dependent on fiber-optic taper. 1:1 shown



Software Solutions

Andor Solis

Solis is a stand alone Windows package with rich functionality for data acquisition and image analysis / processing. Available on 32-bit and 64-bit versions of Windows (XP, Vista, 7 and 8).

Andor Basic provides macro language control of data acquisition, processing, display and export.

Andor SDK (Windows and Linux)

Andor's Software Development Kit allows the user to control the full range of the camera from within your own application.

Available as 32 and 64-bit libraries for Windows (XP, Vista, 7 and 8) as well as Linux. Compatible with C / C++, C#, Delphi, VB6, VB.Net, Labview and Matlab.

Third Party Software

The range of third party software drivers for Andor cameras is always expanding. Please contact Andor for further details.



Accessories

Andor supply a portfolio of accessories to compliment the range of high energy detection products. These range from standard 'off-the-shelf' products, such as recirculators or chillers, to custom-made parts that are designed and manufactured by Andor as part of a specific solution.

The 'O-Y Convertor' flange is an example of an innovative Andor accessory solution, presenting the option to the user of utilising a dedicated 'O' open front vacuum interface in a 'Y' stand-alone mode, with a Beryllium entrance window. Andor also provides custom mounting flanges for all the world's leading VUV / EUV / XUV spectrograph manufacturers; McPherson, Horiba JY and Bruker.

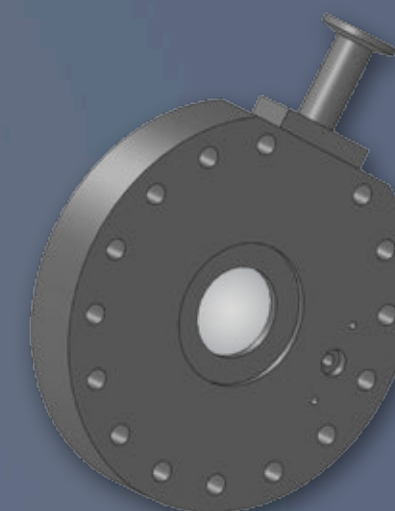
Exotic, custom-built flanges, feedthroughs and other accessory types are available through our Customer Special Request (CSR) service.

O-Y Converter

Use 'Open Front' design camera in 'Stand-Alone' mode. Beryllium window (0.25 mm) as standard. Other window thicknesses or MgF₂ available upon request.

The O-Y Converter is built with a CF-152 flange, designed to be O-ring sealed, with a side mounted KF16 pumpable port.

The window is 60 mm diameter 0.25 mm Beryllium Foil.



Filter Holders and Filters

We supply filter holders designed for a range of environments, including vacuum and fiber-optic. Filters available on request.



Chillers and Recirculators

We offer a range of liquid cooling options to enhance camera performance, either passive or active cooling.



Flanges / Feedthrough

To ease integration into vacuum chambers and connections we offer a range of flanges and feed throughs.



Extender Options

We offer a range of PC connection extender solutions to allow remote operation of our cameras.



Application and Technical Notes

The following section is dedicated to providing a greater depth of understanding of the performance and innovations associated with the Andor high energy camera platforms.

Application Notes

- Monochromatizing a femtosecond high-order harmonic VUV photon source with reflective off-axis zone plates
- Sample analysis with a Grazing Incidence XUV Reflectometer (GIXUVR)
- Single event spectroscopy on laser generated X-Ray beams
- Table-top coherent X-Ray source from mid-infrared high power laser interaction with gases
- A calibrated compact soft X-Ray spectrometer
- Time-Resolved X-Ray diffraction
- Extreme ultraviolet spectroscopy for plasma research
- Neutron radiography / tomography

Technical Notes

- Binning
- Cropped Mode
- Quantum Efficiency (QE)
- Indirect Detection
- Direct Detection

“The combined properties of our custom-built SX-SO436 camera, offering vacuum compatibility and a large area sensor all in one, allows excellent X-Ray imaging with 16-bit resolution. We are happy owners of this versatile instrument.”



Axel Rosenhahn, PhD, BigInterfaces and Holography Group, University of Heidelberg, Germany



Application Note

Monochromatizing a femtosecond high-order harmonic VUV photon source with reflective off-axis zone plates

Introduction

The development of ultra short coherent soft X-Ray pulses paved the way for applications like diffraction microscopy of nanometer structures, ultrafast pump probe spectroscopy, or the investigation of ultrafast atomic, molecular or magnetic phenomena. Of particular interest is high-harmonic generation (HHG). It is a small scale table top source providing ultra-short femtosecond light pulses in the VUV to XUV range. In this process a whole spectrum of distinct wavelengths is released concurrently in one beam. Many applications require this beam to be monochromatized and focused on a target. Here we investigate the optical properties (focal spot, diffraction spectrum, time dispersion and energy resolution) of a so called off-axis reflection zone plate (RZP) that meets these demands with only one optical element. To achieve this, the diffracted light was recorded with an Andor CCD camera.

Experimental Setup

The setup consists of a Ti:Sapphire laser driving the HHG process in a Xenon gas cell. The relevant harmonic spectrum generated in our experiment lies in the range between 15 eV and 45 eV with three prominent peaks at 20.4 eV, 23.6 eV and 26.7 eV. Thus three RZPs were calculated for these energies and were fabricated on a total reflection gold mirror on a silicium substrate. Each RZP focuses its designated energy at the same distance and spot. The RZPs were mounted on a manipulator for alignment and to enable switching between RZPs.

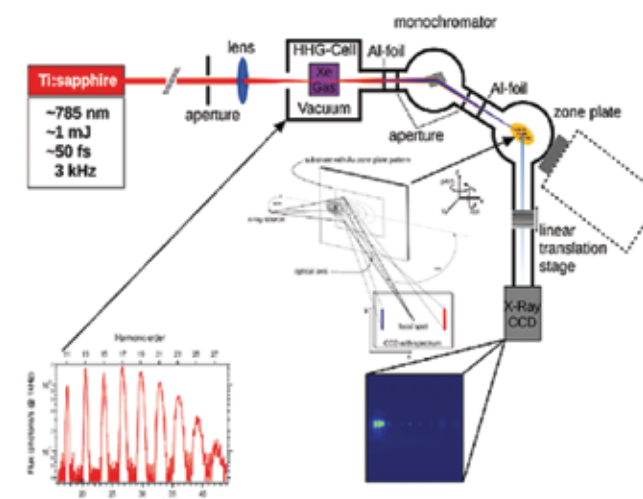


Fig. 1: Experimental Setup

To image the resulting spectra and to investigate the optical properties the highly sensitive Andor X-Ray CCD camera was used (Andor iKon-L DO936N-MW-BN). High sensitivity was necessary due to the low flux of a single harmonic. A shutter connected to the internal trigger of the camera controlled the beam and synchronized it with data acquisition.

Results and Discussion

A RZP basically uses the same principle as the classic Fresnel zone plate, with two distinctions: it works in reflection mode (contrary to transmission mode of classic Fresnel zone plates) and its zone structure is not concentric but as if seen from an angle (here 30°), combining the dispersive properties of a grating and the focusing ability of the Fresnel principle. Fig. 2 shows a typical diffraction spectrum of one of the RZPs and the magnified focal spot. The desired harmonic is focused on the CCD chip whereas the other harmonics are focused before the chip (higher harmonics) or behind the chip (lower harmonics) and thus appear blurry. The chip consists of 2048 x 2048 pixels each measuring 13.5 μm². The large field of view provided visibility of almost all spectral lines/spots without needing to change the orientation of the RZP. At the same time, however the pixel size is small enough to measure reliably the spot size (100 μm - 200 μm) and the distance between harmonics to calculate the energy resolution and dispersion. By comparing intensities of the focal spot and the remainder of the spectrum a determination of the transmission efficiency can be completed. An approximation of the photon flux of the RZP focused VUV light was obtained as the quantum efficiency and and the exposure time was known.

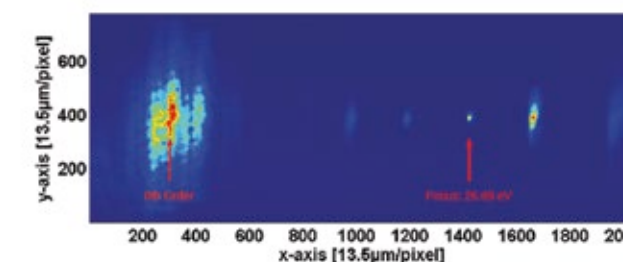


Fig. 2. Full HHG spectrum diffracted by RZP (26.69 eV)

With thanks to:

Mateusz Ibek
Methods and Instrumentation for Synchrotron Radiation Research, Helmholtz Center Berlin for Materials and Energy, Germany

M. Ibek¹, T. Leitner¹, A. Erko², A. Firsov², P. Wernet²
¹ Methods and Instrumentation for Synchrotron Radiation Research, Helmholtz Center Berlin for Materials and Energy
² Nanometer Optics and Technology, Helmholtz Center Berlin for Materials and Energy (February 2011)

Application Note

Sample analysis with a grazing incidence XUV reflectometer (GIXUVR)

Introduction

The group 'Technology of extreme ultraviolet radiation' at Chair Technology of Optical Systems (TOS), the RWTH Aachen, Germany, investigates applications for laboratory-based XUV gas-discharge sources [1]. Extreme ultraviolet radiation (XUV, 1-50 nm, or EUV at 13.5 nm) enables new optical, analytical and manufacturing technologies because of its characteristic interaction with matter, its short wavelength, and recent progress on light sources and optical components. XUV tools are already deployed by the semiconductor industry in the next generation lithography, which significantly accelerates a further development of XUV technology. Future applications that will support the scientific progress in a variety of fields, such as nanoelectronics or bio-technology, are the scope of their research. Activities include structuring on a nanometer scale using interference lithography, XUV microscopy for imaging of dynamic processes or at-wavelength inspection of multilayer mask-blanks for hidden defects, and characterization of thin film coated surfaces using grazing-incidence reflectometry [2-6].

For the detection of the XUV radiation charge coupled devices (CCDs) with sufficient quantum efficiency at the XUV wavelengths and with low level of noise are needed. Therefore several Andor CCD cameras are used in the group's laboratories.

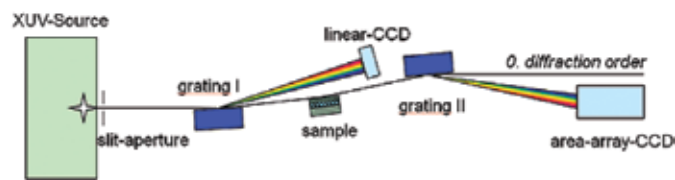


Fig. 1: Schematic of the grazing incidence XUV reflectometer (GIXUVR)

XUV Reflectometer

The reflectometry set into the Andor DX440-BN CCD is successfully integrated. The developed XUV reflectometer, shown in Fig. 1 and Fig. 2, consists of two spectrometers.

The first spectrometer utilizes a compact backthinned line sensor with the purpose of determining the source emission spectrum. After interaction of the zeroth order of the emission with the sample, the spectrum is analyzed again with the Andor CCD at the end of the beamline. A typical measured line spectrum is shown in the Fig. 3. The DX440-BN also offers the possibility of in-vacuum operation that allow the researchers to perform additional measurements of the scattered radiation.

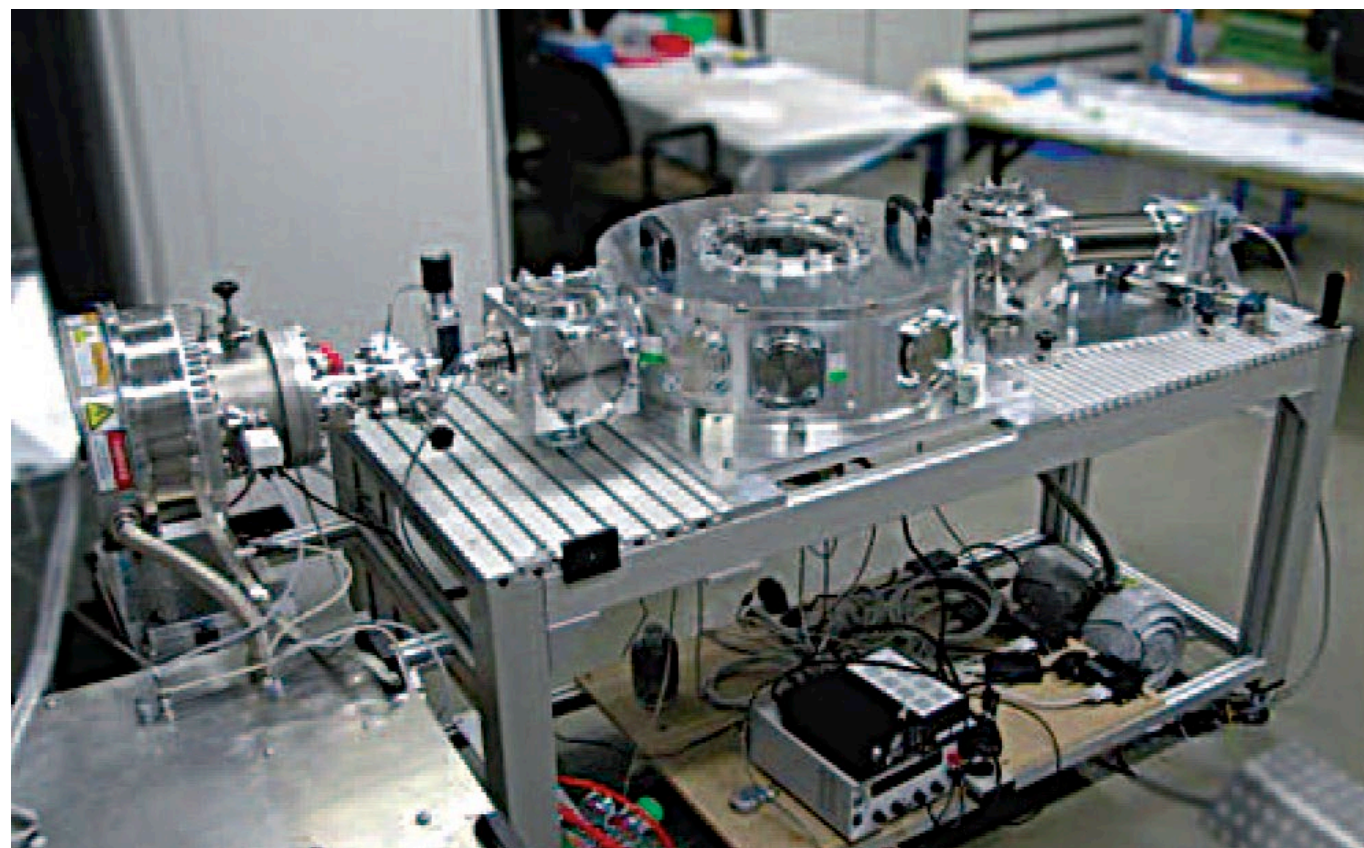


Fig. 2: Photo of the GIXUVR at the RWTH Aachen

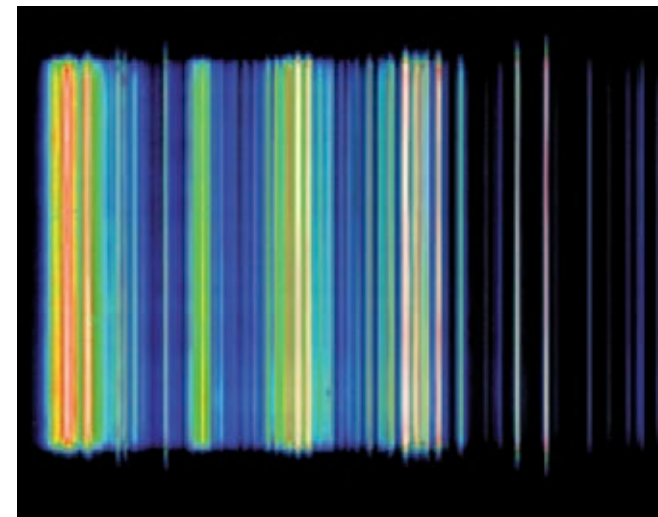


Fig. 3: Line spectrum of the emission of a gas-discharge XUV source measured by the Andor DX440-BN CCD camera

The pixel size of $13.5 \times 13.5 \mu\text{m}^2$ provides a state-of-the-art resolution at this wavelength range. With a sensor size of 2048×512 pixels the CCD allows for excellent spectral resolution, as well as a capability to average the signal over 512 lines, thus improving the accuracy of measurements. In comparison to line sensors, which were also investigated, the CCD offers the possibility of a vertical adjustment [7].

XUV Quantum Efficiency

Series of experiments were performed with the Physikalische Technische Bundesanstalt (PTB) at the synchrotron BESSY in Berlin, Germany, to determine the quantum efficiency at the XUV wavelengths. The quantum efficiency of the Andor DX440-BN CCD in the range from 1 nm to 34 nm is shown in Fig. 4.

The maximum of the QE is at 27 nm wavelength with the value of 64.6%. Due to strong absorption of XUV radiation at the L-absorption edge of silicon a local minimum of 26.8% is situated next to 12.4 nm [8].

In summary, the research group found the Andor DX440-BN detector offers good quantum efficiency in the XUV regime and provides a state-of-the-art resolution.

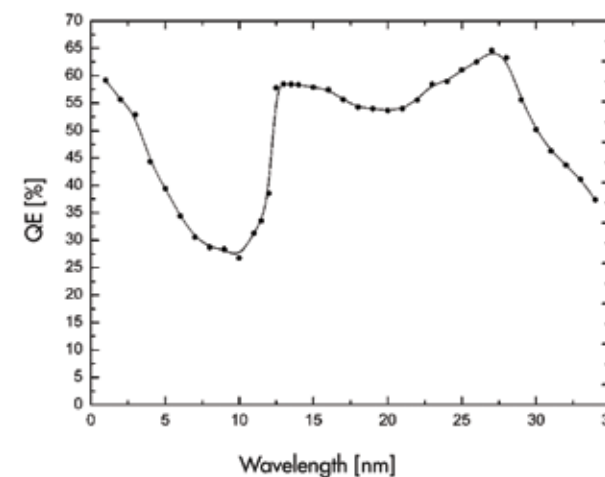


Fig. 4: Determined quantum efficiency of the Andor DX440-BN CCD detector from 1 nm to 34 nm wavelength

With thanks to:

Dipl.-Ing. (FH) Sascha Brose
Chair for the Technology of Optical Systems
RWTH Aachen University, Germany

- [1] K. Bergmann, S.V. Danylyuk, L. Juschkina, 'Optimization of a gas discharge plasma source for extreme ultraviolet interference lithography at a wavelength of 11 nm', *J. Appl. Phys.* 106, 073309–073309-5 (2009)
- [2] S. Danylyuk, L. Juschkina, S. Brose, K. Bergmann, P. Loosen, J. Moers, S. Trellenkamp, G. Panaitov, K. Wambach and D. Grützmacher, 'XUV interference lithography for sub-10 nm patterning', *Jülich-Aachen Research Alliance - annual report 2008*, pp. 49–50 (2009)
- [3] L. Juschkina, R. Freiberger, K. Bergmann, 'EUV microscopy for defect inspection by dark-field mapping and zone plate zooming', *Journal of Physics: CS* 186, 012030–012030-3 (2009)
- [4] S. Herbert, A. Maryasov, L. Juschkina, R. Lebert, K. Bergmann, 'Defect inspection with an EUV microscope', in '26th European Mask and Lithography Conference' edited by U. F. W. Behringer and W. Maurer, *Proc. SPIE* 7545, 75450O–75450O-9 (2010)
- [5] M. Banyay, L. Juschkina, 'Table-top reflectometer in the extreme ultraviolet for surface sensitive analysis', *Applied Physics Letters* 94 (6), id. 063507 (2009)
- [6] M. Banyay, L. Juschkina, 'Spectral sharpening algorithm for a polychromatic reflectometer in the extreme ultraviolet', *Applied Spectroscopy* 64 (4), 401–408 (2010)
- [7] M. Banyay, S. Brose, L. Juschkina, 'Line image sensors for spectroscopic applications in the extreme ultraviolet', *Meas. Sci. Technol.* 20, 105201–105201-5 (2009)
- [8] S. Brose, 'Experimentelle Untersuchungen zur Adaption von Zeilendetektoren für Anwendungen extreme ultravioletter Strahlung', diploma thesis, FH Aachen, Jülich (2008)

Application Note

Single event spectroscopy on laser generated X-Ray beams

Introduction

The use of ultra intense laser pulses to excite plasma waves with a relativistic phase velocity is a possible route to the development of compact particle accelerators.

Quasi-monoenergetic electron beams with energies from 0.1 to 1 GeV have been reliably generated [1,2]. In addition, these compact particle accelerators are sources of intense X-Rays with peak brilliances comparable to ‘3rd generation’ synchrotrons [4]. The electrons in the laser driven wakefield do not only experience a strong accelerating field but also a strong focusing field, forcing them to oscillate transversally in so called ‘betatron orbits’ [3]. The pulse is perfectly synchronized with the driving laser pulse; the duration of the generated X-Rays is of the same order as its pulse duration [5]. These unique properties offer the opportunity to investigate ultrafast processes in solids or warm dense matter using femtosecond X-Ray diffraction or time-resolved absorption spectroscopy (NEXAFS / EXAFS).

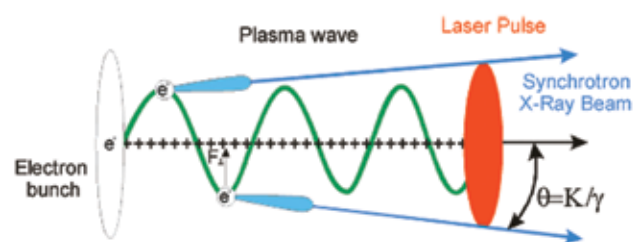


Fig. 1 Schematic of the production of short X-Ray pulses by betatron oscillation inside a plasma

X-Ray sources of this type are based on the betatron oscillation of a relativistic electron in a laser-produced plasma wave. Large numbers of these electrons are bunched together by the interaction with the driving field. Electrons inside each bunch are accelerated longitudinally with the propagating pulse. Additionally they experience the transverse electrostatic field within the wave, much as fast electrons experience periodic magnetic forces inside a synchrotron. The transverse acceleration leads to betatron oscillations. The result is a collimated beam of broadband radiation in the X-Ray range, which is emitted at femtosecond pulse lengths. The spectrum and maximum achievable photon energy is determined by the laser and gas parameters.

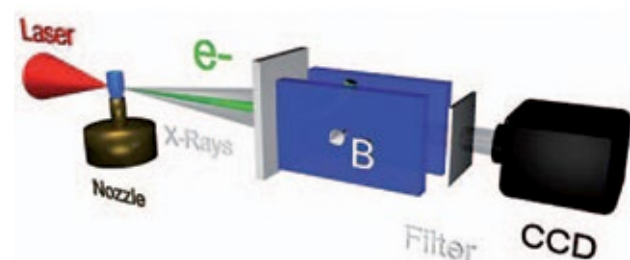


Fig. 2 Experimental setup for the detection and characterization of betatron radiation from laser-plasma-interaction in a He gas jet

Setup

As a driving laser, the JETI laser system at the Institute of Optics and Quantum Electronics in Jena is a multistage CPA system, based on a titanium doped sapphire, which emits at 800 nm central wavelength.

Pulse energies up to 0.7 J of 30 fs duration were used for these experiments. This corresponds to peak intensities inside the target slightly above 1018 W/cm². The laser is focused into a supersonic Helium gas-jet (Fig. 2). The spectrum of the laser accelerated electrons was measured by deflecting the electrons with a 0.5 T permanent magnet onto lanex screens (not shown in Fig. 2). The emitted X-Rays are recorded by a CCD. This scheme allows the researcher to correlate the energy spectrum of the electrons with the energy of emitted photons for single shot experiments.

In order to characterize the emitted X-Rays a large area back-illuminated CCD (iKon-L DO936NMW-BN) was used. Thin filters were placed in front of the CCD to block radiation below 1 keV. The camera was calibrated for single photon event spectroscopy from well-defined classical X-Ray sources. The count number of single events is assigned to a characteristic photon energy. The small pixel size (13.5 x 13.5 μm²) allows reasonable resolution, while the separation of neighboring events is still possible.

The spatial resolution and high dynamic range can be useful when determining the spatial geometric properties of the source, e.g. by projecting the shadow image of a wire of known diameter onto the chip. In this way the source was determined to be smaller than 14 μm in diameter.

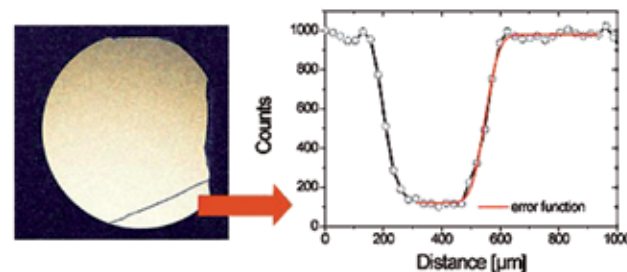


Fig. 3 Determination of the X-Ray source size by evaluating the shadow thrown by a narrow wire projected on the CCD

Experimental results

So far, more than 10,000 single shot images have been taken in this setup. From one image a typical X-Ray spectrum of the source can be reconstructed. The results are shown in Fig. 4. Photons of energies up to 10 keV, with a maximum in the spectrum around 2 keV. The low energy cutoff is given by the transmission of the used filters. Accounting for the filter function by deconvolution, the results agree reasonably well with simulations.

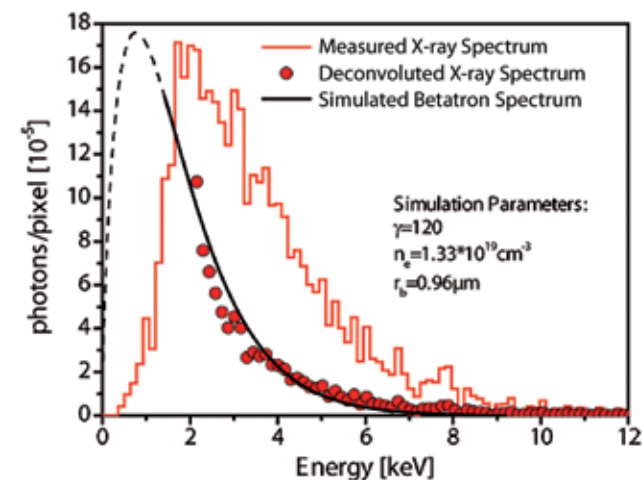


Fig. 4 X-Ray spectrum of the betatron source

Summary and Outlook

First experiments have successfully demonstrated the generation of broadband betatron radiation with photon energies of several keV. In the future, density shaped plasmas will be investigated to generate X-Rays with even higher photon energies. The long term goal is the use of betatron radiation for ultrafast time-resolved absorption spectroscopy. This work is funded as a subproject of the SFB Transregio 18.

With thanks to:

Michael Schnell, Institute of Optics and Quantum Electronics University of Jena, Germany

- [1] Leemans et al., Nat. Phys. 2 696 (2006)
- [2] Kneip et al., PRL 103, 035002 (2009)
- [3] Rousse et al., PRL 93 (2004)
- [4] Kneip et al., PRL 100, 105006 (2008)
- [5] K.Ta Phuoc et al., Phys. Plasmas, 14, 080701 (2007)

Application Note

Table-top coherent X-Ray source from mid-infrared high power laser interaction with gases

Introduction

The unique ability of X-Rays for elemental and chemically-specific imaging of thick samples at the nanoscale have spurred the development of X-Ray free-electron laser sources, as well as ultrafast high harmonic (HHG) X-Rays, from tabletop-scale femtosecond lasers. The unprecedented femtosecond-to-attosecond pulse duration and full spatial coherence of the HHG light make it possible to capture the motions of electrons, atoms, and molecules in real time, to observe element-specific dynamics at the M-shell absorption edges of magnetic materials, to understand heat flow in nanostructures, and to implement table-top microscopes with record spatial resolutions of 20 nm.

However, to date, most applications that use HHG light have been limited to the extreme ultraviolet (EUV) region of the spectrum, ~50 – 100 eV. Extending HHG to photon energies into the keV region would open up a host of important applications in probing thicker samples (since matter is more transparent at higher photon energies), capturing dynamics at the L-edges of magnetic materials, and imaging dynamics with nanometer-scale spatial resolution. The grand challenge for extending bright HHG to higher energies is the development of phase matching techniques that enable efficient nonlinear upconversion. In previous research using mid-infrared lasers at wavelengths up to 2 μm to drive HHG, full phase matching

was demonstrated in the water window up to photon energies of 0.52 keV [1-4]. Essentially, the macroscopic full phase matching cutoff energy scales almost as strongly with the wavelength of the driving laser, $h\nu_{\text{PM}} \text{ cutoff} \propto \lambda_L(1.5-1.7)$, as with the microscopic single-atom cutoff, $h\nu_{\text{SA}} \text{ cutoff} \propto \lambda_L^2$. The research group demonstrated bright coherent HHG X-Rays at photon energies >1.6 keV (<7.8 \AA), promising to realize a coherent ultrafast implementation of the Roentgen X-Ray tube in a tabletop-scale apparatus. Full phase matching of HHG in the keV region of the spectrum (> 5031th order) is possible for the first time by using driving laser wavelengths around 3.9 μm . In addition, it generates the broadest coherent supercontinuum to date of >1.3 keV, from any light source, large or small scale.

Experimental Setup

In this experiment, 6-cycle FWHM, 3.9 μm , 20 Hz, multi-mJ pulses are generated as the idler from a novel optical parametric chirped-pulse amplification (OPCPA) architecture. The front end of the OPCPA is based on a femtosecond Yb:CaF₂ chirped pulse amplifier that drives a cascaded femtosecond OPA. The subsequent KTA stages of the OPCPA are pumped by a 20 Hz picosecond Nd:YAG laser system and produce uncompressed 30 mJ and compressed 8.5 mJ energy in the signal and the idler beams at 1.46 μm and 3.9 μm ,

respectively - the highest pulse energy from a femtosecond mid-IR source to date. HHG X-Rays are generated by guiding the ultrafast laser beams in a hollow waveguide designed to hold multi-atm phase-matching pressure gases. A custom-made grating spectrometer is used for spectral analysis of generated radiation. X-Ray HHG spectra are acquired using the highly-sensitive X-Ray CCD camera Newton DO920N-BN, (Andor Technology), cooled down to -50 $^{\circ}\text{C}$ to minimize noise.

Experimental results

Using 3.9 μm pulses and 35 atm of He as a nonlinear medium, Fig. 1 shows that the phase matched emission extends to >1.6 keV (<7.8 \AA), representing an extreme for coherent frequency upconversion - up to order > 5031th. Fig. 2A shows that the HHG X-Ray signal grows quadratically with pressure, even in very dense gas media (with low ionization levels of 0.03%). An approximate brightness corresponding to 108 photons/sec at 1 kHz is observed in a fractional bandwidth of 1% at 1 keV, which is 4 to 5 orders of magnitude greater than reported using 0.8 μm drivers. Full phase matching in Ar, molecular N₂, and Ne are restricted by absorption at their L- and K-shell absorption edges of 0.254 keV, 0.41 keV and 0.87 keV (see Fig. 2C). The observed HHG emission from N₂ is the highest observed from any molecule to date and has potential for tomographic orbital reconstruction. Finally, to illustrate also the wide breadth of the element-specificity of the keV supercontinuum from this tabletop coherent source, L absorption edges of metals were recorded, including magnetic materials, through the soft X-ray region, as shown in Fig.2B.

Conclusion

In summary, this study has demonstrated fully phase-matched X-Ray generation in the kiloelectronvolt photon energy region (sub-1 nm wavelengths) for the first time. At 1 kHz, the photon flux that would correspond to ~108 photons / sec in a fractional bandwidth of $\Delta\lambda/\lambda \approx 1\%$ at 1 keV, which is sufficient to enable static and ultrafast bio- and nano-imaging in the water window and beyond, and element-selective magnetic imaging at 0.7–0.9 keV.

With thanks to:

Dr. Daniil Kartashov, Photonics Institute, Vienna University of Technology, Austria

- [1] T. Popmintchev et al., *Opt. Lett.* 33, 2128 (2008).
- [2] T. Popmintchev et al., *PNAS* 106, 10516 (2009).
- [3] M.C. Chen et al., *Phys. Rev. Lett.* 105, 173901 (2010).
- [4] T. Popmintchev et al., *Nature Photonics* 4, 822-832 (2010).

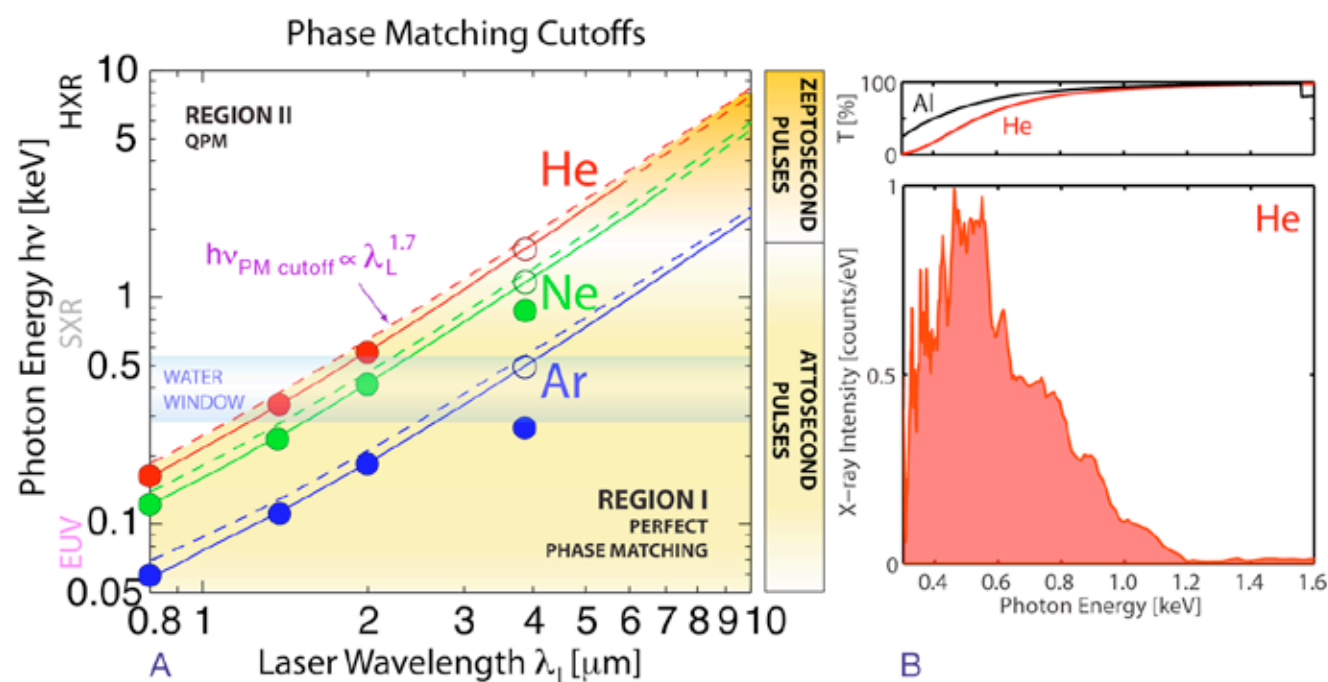


Fig. 1. A. Predicted HHG full phase matching cutoffs as a function of the driving laser wavelength, below which bright HHG emission is possible. This generalized phase matching picture is here validated to above 1 keV. Solid circles represent current experimental results and open circles represent the theoretically expected phase matching limits. As predicted [1], X-Rays from Ar and Ne cannot reach the phase matching cutoffs due to L (0.254 keV) and K (0.870 keV) shell absorptions. The absence of inner shell absorption in He allows for the generation of keV X-Rays. B. Fully phase matched X-Ray supercontinuum to >1.6 keV or 7.8 \AA (note linear X-Ray intensity scale) with bandwidth >1.3 keV (tail to tail).

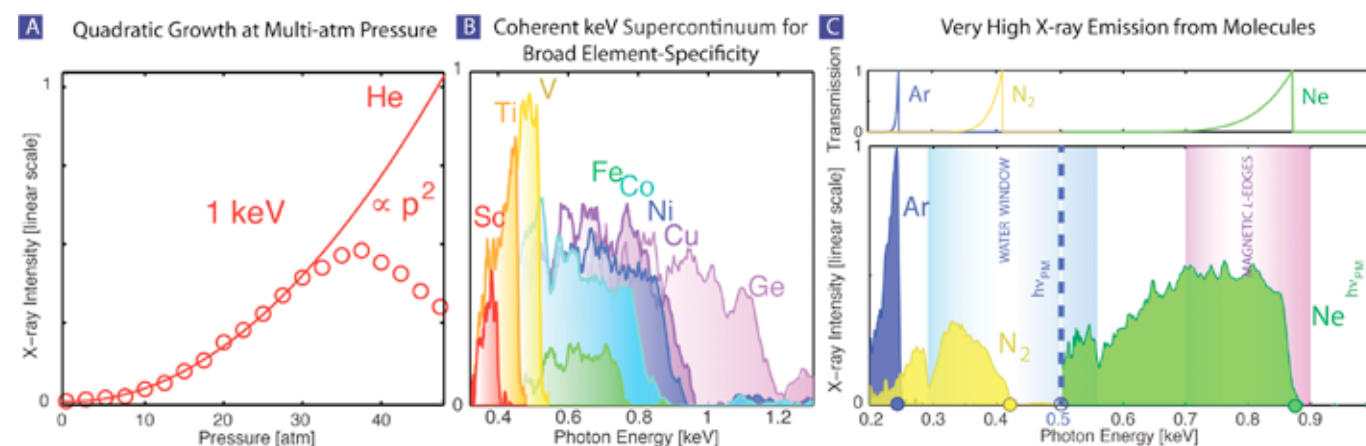


Fig. 2 A. The experimental X-Ray signal at 1 keV grows quadratically with pressure showing excellent coherent buildup in dense, 40 atm, gas pressures where the rescattering electron can encounter neutral atoms and ions. Fig. 2 B. Measured L-absorption edges of metals, including magnetic materials, throughout the soft X-Ray region, demonstrating a useful probe for femtosecond-to-attosecond element-selective spectroscopies. Fig. 2 C. X-Ray emission from Ar and N₂ (similar ionization potentials), and Ne. The predicted phase matching cutoffs $h\nu_{\text{PM}}$ (dashed vertical lines) cannot be reached due to reabsorption of the generated X-Rays at the L- and K-shell absorption edges (0.254 keV - Ar, 0.41 keV - N₂, 0.87 keV - Ne). The 0.41 keV phase-matched X-Rays from N₂ in the water window represents the highest HHG photon energy obtained from molecules to date.

Application Note

A Calibrated Compact Soft X-Ray Spectrometer

Introduction

Laser-produced plasma sources for the soft X-Ray region (1 - 20 nm corresponding to a photon energy between 1200 eV - 60 eV) are widely used in spectroscopy, extreme ultraviolet (EUV) lithography and X-Ray imaging. To qualify these sources, the emitted absolute photon numbers are of special interest. The characterization of the spectral emission of the source is crucial e.g. in EUV lithography or in X-Ray microscopy. In both cases, the control of the exposure process requires the exact knowledge of the photon numbers. Various kinds of spectrometers have been developed and applied to characterize laser-produced plasmas. A very compact spectrometer consisting of a transmission grating, a slit and a back-illuminated CCD camera was firstly proposed by Wilhein [1].

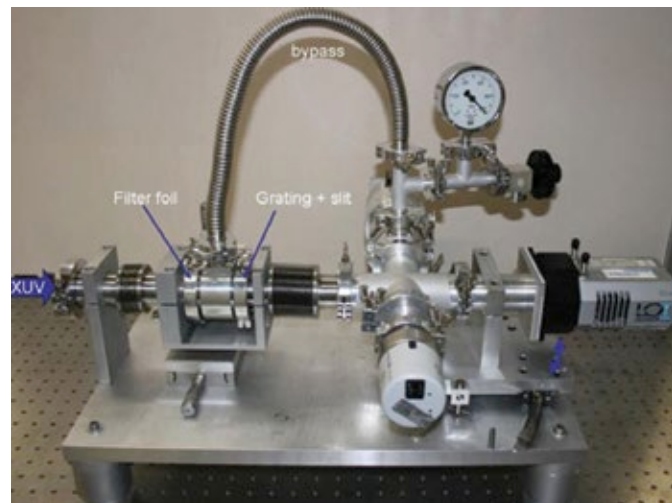


Fig. 1 Photograph showing the compact transmission grating spectrometer together with an Andor iDus X-Ray CCD detector.

Setup

The working principle of the soft X-Ray spectrometer is very simple: the X-Ray source projects a shadow of the grating-carrying slit onto the detector. In the detector plane a diffraction pattern occurs at position $x = \lambda B/D$ with λ : wavelength, B: distance grating-detector and D: grating period. For a compact soft X-Ray spectrometer (Fig. 1) the research group used a setup similar to [1]. The spectrometer consists of a filter (thin Al, Cr or Ti foil) for the suppression of VIS/NIR light originating from the laser, a transmission grating (10,000 l/mm), a slit (500 μm x 50 μm) and a back-illuminated X-Ray CCD camera DO420A-BN with 1024 x 255 pixels (pixel size 26 μm) from Andor Technology. In order to make the whole setup very compact and to make the alignment easy all X-Ray optics were placed inside standard KF40 flanges. The CCD camera was delivered by Andor with a space saving custom flange.

Using a self made interface flange it was possible to connect the CCD camera directly with KF40 tubes to the vacuum system. In order to choose easily the desired wavelength region, the CCD camera was attached to a stage moving on a bar (Fig. 1). The whole

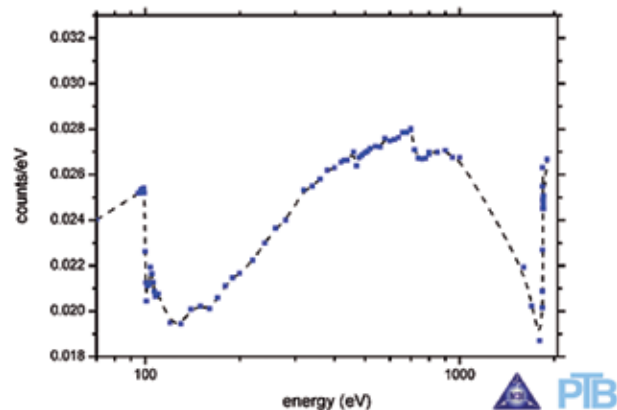


Fig. 2 Spectral sensitivity of the Andor back-illuminated CCD camera DO420A-BN with 1024 x 255 pixels measured at PTB BESSYII beamline Berlin.

setup fits to a base plate of 300 mm x 500 mm. It was completed by a small turbo pump (Pfeiffer Vacuum) to guarantee a base pressure in the spectrometer of 10⁻⁶ mbar. All measurements were carried out with a cooled down CCD camera chip at -45 °C.

Calibration

The calibration procedure for the CCD camera, as well as for the transmission grating, was performed at the radiometry PTB BESSY II beamline. In a first step the CCD camera was calibrated within an photon energy range of 70 - 1900 eV (corresponding to a wavelength region 18 - 0.7 nm). The results are shown in Fig. 2. The average error of the calibration procedure was < 5%. In a second step the slit and the transmission grating were added and the relative intensities of zero and first order diffraction patterns were obtained. From these data the grating efficiency in the range 100 - 600 eV corresponding to a wavelength region 12 - 2 nm was calculated. It was found that the experimental curve (data not shown) in principle follows the grating efficiency calculated using the Henke data [2], taking into account a thickness of the grating support of about 100 nm. The maximum grating efficiency in the water window (2.2 - 4.4 nm) amounts to 0.015 with an average error of about 20%. The transmission of the filters (Cr, Ti) used in the experiments to block the visible light of the laser was determined 'at wavelength' comparing the counts on CCD camera with and without filter.

Application

The compact transmission grating spectrometer was applied to experiments with a liquid nitrogen jet [3] target system. The driving laser was a Nd:YAG laser (Quantel BRILLIANT) with 3 ns, 120 mJ, 10 Hz output at 1064 nm focused to a 15 μm diameter spot, resulting in an intensity of 3×10^{13} W/cm² applied to the liquid nitrogen jet. The grating was placed in a distance of about 500 mm from the source. Together with a grating-detector distance of 400 mm and

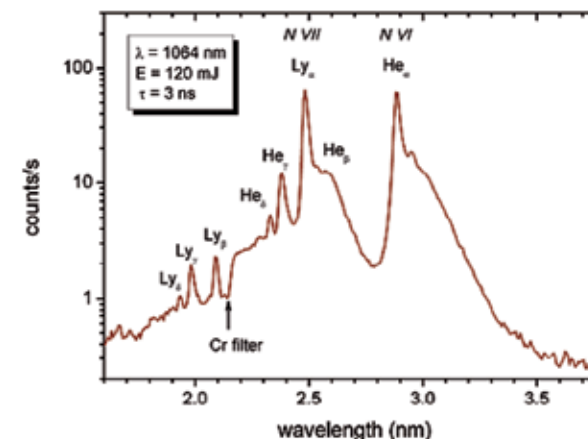


Fig. 3 Liquid-nitrogen-jet laser-plasma emission spectrum measured with the compact transmission grating spectrometer.

a source size of about 20 μm the calculated spectral resolution [1] amounts to $\lambda/\Delta\lambda = 100$ at 2.48 nm, the design wavelength of the laser plasma source.

The measured spectrum is shown in Fig. 3. The spectrum consists of different lines assigned to different ionization stages of nitrogen. Two series are observed: the H like emission lines of N-VII ions and the He like emission lines of N-VI ions. From the experimental data a linewidth of 0.02 nm for the Ly- α line corresponding to a spectral resolution of about 100 was found in agreement with the calculated value. Using the calibration data for the CCD camera, the grating and the Cr filter the photon flux was estimated to 4×10^{11} ph/pulse sr for the He- α line and 3×10^{11} ph/pulse sr for the Ly- α line.

With thanks to:

H. Stiel and H. Legall, Max-Born Institut für Nichtlineare Optik und Kurzzeitspektroskopie Berlin, Germany

[1] Wilhein, T., et al., A slit grating spectrograph for quantitative soft X-Ray spectroscopy. *Rev. of Sci. Instrum.*, 1999. 70(3): p. 1694-1699.

[2] Henke, B.L., http://henke.lbl.gov/optical_constants.

[3] Jansson, P.A.C., U. Vogt, and H.M. Hertz, Liquid-nitrogen-jet laser-plasma source for compact soft X-Ray microscopy. *Rev. Sci. Instrum.*, 2005. 76(4): p. 043503/1-5.

Application Note

Time-Resolved X-Ray Diffraction

Introduction

In recent years a new method has been developed to study the time evolution of atomic and molecular structure on the time scale of 100 femtosecond ($1\text{fs}=10^{-15}\text{s}$), which is the typical time scale for atomic vibration. This method will give new insights of the temporal evolution of physical, chemical and biological processes on the atomic scale. New developments, such as new X-Ray sources, femtosecond lasers, and X-Ray optics, were essential for this study. But without new detector development in the keV-photon range such experiments are not possible. A combination of a toroidally bent crystal optics with a CCD camera can provide the simultaneous measurement of transient crystal diffraction curves [1].

Time-Resolved X-Ray diffraction using a pulsed femtosecond X-Ray source at Institut für Optik und Quantenelektronik, in Jena

A typical set up for Time-Resolved diffraction is shown in Fig. 1. The interaction of short intense laser pulses ($t=100\text{fs}$, $I>10^{15}\text{W/cm}^2$) with solid matter creates a thin dense plasma layer where electrons can be efficiently accelerated to keV or even MeV energies. Such electrons can produce short X-Ray pulses when interacting with a solid. The X-Ray source is slightly larger than the laser focus, typically produced some tens of micrometers. Intense line

radiation from the laser based X-Ray source, like $K\alpha$ lines, are being focussed with toroidally bent crystals onto the samples which are investigated. Then a spherical monochromatic wave is falling on the sample. The diffracted X-Ray signal from the sample (Fig. 2a) is recorded by an Andor back-illuminated, deep depletion X-Ray CCD camera, a DX420-BR-DD with 1024×255 pixels, providing the rocking curve in the case of a single crystal sample (Fig. 2b). Excitation of the sample by a second laser pulse with a certain delay before the X-Ray probe pulse, allows researchers to follow the temporal response of the diffraction signal by varying the delay of both pulses [2].

Properties of X-Ray CCD cameras

Important properties of back-illuminated deep depletion CCDs have the following advantages compared to other X-Ray detectors [3]:

- Accumulation of photons over various exposures (typically 1 s - 1,000 s) due to the camera's low sensor temperature.
- Detection of single photon events in the keV-photon- energy range. More than 250,000 single solid state detectors, each pixel, record simultaneously the signal.
- High detection efficiency, more than 90% for 4.5 keV photons.
- Retain excellent linearity between photon energy and

detected charge.

- The photon energy can be reconstructed, even if the charge of one photon is split into four pixels.
- The CCD cameras can be used in a vacuum experiment as well as in small flexible vacuum housings (see Fig. 1)
- Relatively low mass, easily translated and rotated.

Application for Time-Resolved experiments

Time-Resolved experiments require significant properties of the detectors to record successfully reasonable data. One of the most important parameters for these experiments is the time average X-Ray photon flux. A high detection efficiency reduces the extremely high cost for a high average power of the femtosecond laser driving the X-Ray source.

X-Ray CCDs are applied in various steps of these experiments:

- As a recording X-Ray spectrometer in the single photon counting mode (line spectra and Bremsstrahlung), for laser based X-Ray source optimization
- With CCDs, online alignment of the X-Ray optics (i.e. toroidally bent crystals) can be completed, for example, Bragg angle rotation, crystal azimuth rotation and focus alignment.
- Crystal rocking curves, transient or static, are recorded from crystal samples (Fig. 2 (b)).

Advantages for data analysis using back-illuminated deep depletion X-Ray CCD cameras are:

- Diffracted single photons can be located with a precision of one pixel. This corresponds to an angular resolution of typical 0.5 arcminute in diffraction experiments.
- The background level given by the CCD temperature can be subtracted relatively easily.
- Scattered hard photons not contributing to the diffracted signal, but disturbing the measurement can be easily removed if single photon counting mode is used.
- The reconstruction of the rocking curve from the two-dimensional CCD image (Kossel cone in Fig. 2a).
- Ability to record large solid angles diffracted by the samples due to the large detector area.

With thanks to:

1. *Uschmann, Institut für Optik und Quantenelektronik, Friedrich-Schiller-Universität Jena, Germany*

1. *Ch. Rischel, et al., Nature 390, 490 (1997).*

2. *A. Morak, et al., Phys. Stat. Sol., No. pssb.200642387, (2006).*

3. *F. Zamponi, et al., Rev. Sci. Instrum., 76, 116101 (2005).*

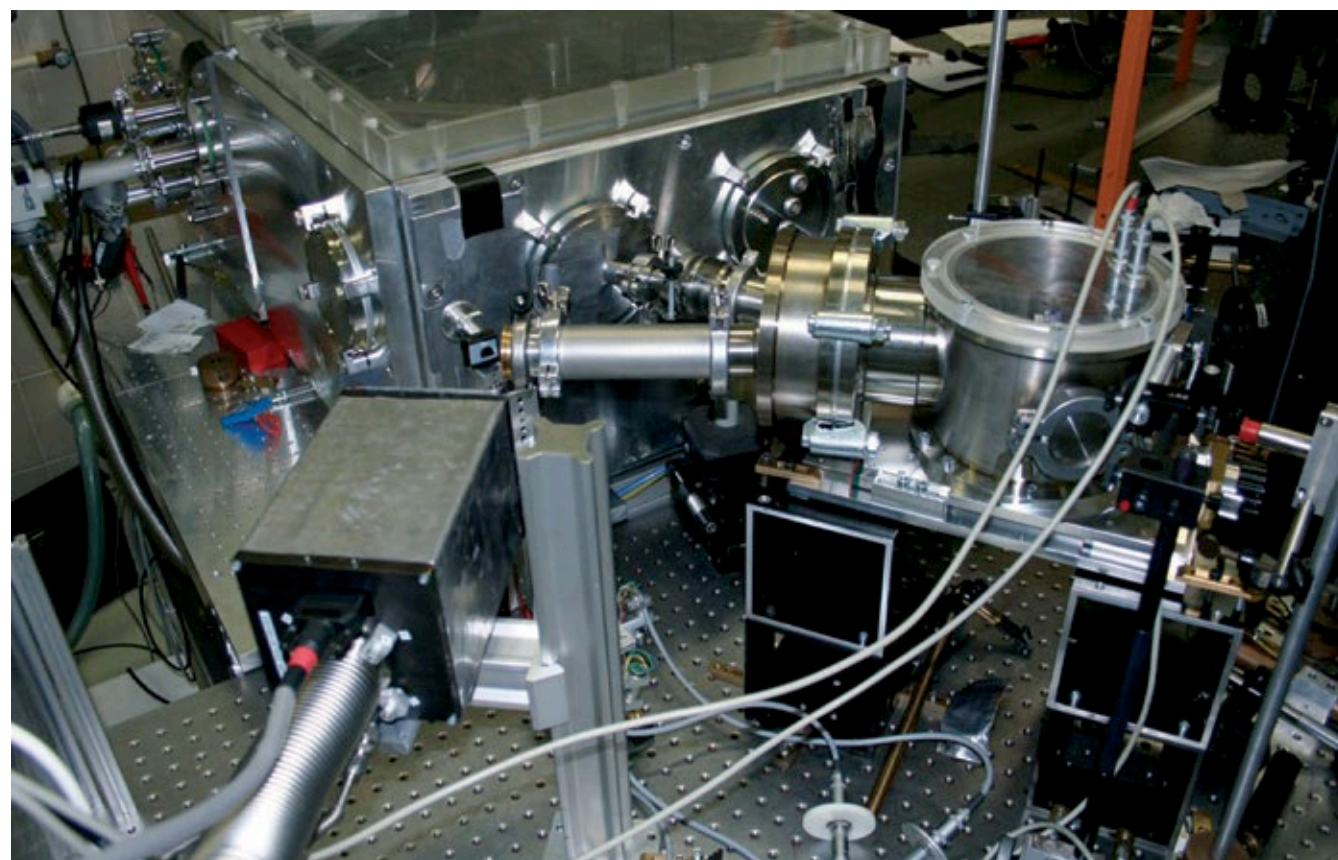


Fig. 1. Time-Resolved X-Ray diffraction setup

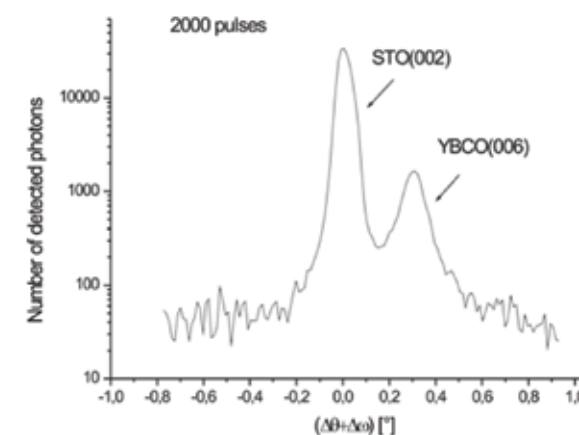


Fig. 2 (b). A single crystal rocking curve

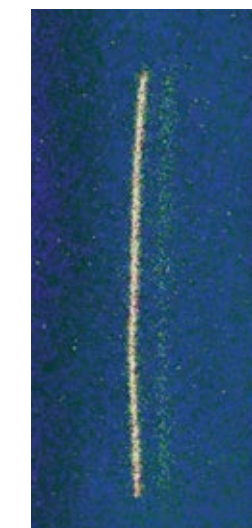


Fig. 2(a) - Kossel Cone CCD image

Application Note

Extreme Ultraviolet Spectroscopy for Plasma Research

Researchers around the world are studying fusion as a potential source of energy. Fusion is considered to be safer than today's nuclear fission power plants because it can occur only under very limited and controlled circumstances. However, fusion is very much still in the research stage.

Dr. Shigeru Morita of the National Institute for Fusion Science in Japan is part of a group of researchers involved in magnetically-confined plasma research. 'We need a large effort over a long time to realize a fusion reactor,' Dr. Morita said. 'But I believe that fusion is the best solution to yield electricity for the future.'

One way to perform fusion is with magnet confinement, which uses magnetic fields to confine the hot fusion fuel in the form of a plasma. The researchers want to understand impurity transport in magnetically-confined plasmas in order to better control impurities in the fusion plasma. Impurities can cause radiation loss and affect fuel dilution, causing a reduction in the fusion energy output.

Most impurities emitted from the fusion plasma require spectroscopic detection in the extreme ultraviolet (EUV) wavelength range (10 to 500 Angstrom or 1 to 50 nm), which can pose a challenge for detection. Because the researchers were studying impurities in magnetically-confined plasmas in the large helical device (LHD) at the National Institute of Fusion Science, they also needed a relatively large detection area in order to observe the 1-m radial profile of the LHD plasma.

Previously the researchers had used a microchannel plate (MCP) combined with a photodiode array for EUV spectroscopy, but this set up exhibited a high amount of thermal noise and poor spatial resolution. To use a CCD detector for EUV spectroscopy would require the sensor to be uncoated and to be fairly large. For these reasons the researchers turned to the Andor DO420-BN CCD camera to meet these requirements. 'Using the back-illuminated CCD for the detection of EUV light worked very well and showed much less thermal noise, good spatial resolution and a high count rate,' Dr. Morita said. 'It dramatically changed the EUV spectroscopy performed in the fusion study.'

The sensor in the Andor DO420-BN CCD camera is back-illuminated with no anti-reflection coating. The 1024 x 255 array with pixel size of 26 x 26 μm^2 gives an active area of 26.6 x 6.6 mm. The researchers incorporated this camera into a EUV spectrometer system consisting of an entrance slit, a spatial resolution slit, and a gold-coated concave varied-line-spacing (VLS) grating. The CCD can be cooled to -70 °C to reduce the thermal noise, but the researchers typically operated it at -20 °C, which provided sufficiently reduced thermal noise.

They placed the CCD vertically at the focal plane of the spectrometer, so the vertical profile was recorded along the CCD's long axis (z axis: 26.6 mm, 1024 pixels), and the spectrum was recorded along the CCD's short axis (x axis: 6.6 mm, 255 pixels). They used the camera in full resolution image mode for the spectral

resolution test and for the line identification. This mode delivers the best spectral resolution but requires a longer exposure time. For routine measurements of the impurities, they used the camera's cropped mode function.

'Using the Andor DO420-BN CCD camera, we could observe the radial profile of impurity line emission from LHD fusion plasmas in EUV range to study the impurity transport,' Dr. Morita said. 'This was the first time in magnetic confinement fusion research that the radial profile was observed in EUV range with such good results.'

The researchers used the space-resolved EUV spectrometer to measure the radial profiles of impurity ions of carbon, neon and iron for high-temperature plasmas in a large helical device (LHD). The measurements were performed in the wavelength range of 60 to 400 Angstroms and revealed information not previously known about the plasma impurities. For example, they found that impurity ions with ionization energies between 0.3 and 1.0 keV were located in the outer region of plasma while those with ionization energies of less than or equal to 0.3 keV were located in the ergodic layer.

Importantly, they also found that the electron temperature is approximately equal to ionization energy for impurity ions with ionization energy less than or equal to 0.3 keV, while impurity ions with ionization energies between 0.3 and 1.0 keV have an electron temperature roughly half that of their ionization energy. This likely occurs because of the difference in transverse transport between the plasma edge and the ergodic layer. Combining this information with other results allowed the researchers to qualitatively explain the differences in the impurity radial positions.

They also carefully examined the peak position of CIV, which was identified as the ion existing in the farthest edge of the ergodic layer. It was found that the position moves inside the ergodic layer when the edge electron temperature was reduced below a threshold temperature, e.g. where it does not change at all in a temperature range above the threshold. This indicated that the edge boundary of LHD was determined by a starting point of the open field layer near the O-point, not the X-point. Comparison with a three-dimensional edge transport code in the CIV peak position showed a clear discrepancy of 8 mm, suggesting a modification of the stochastic edge magnetic field due to the presence of plasma pressure.

Research Papers:

- 1) Chunfeng Dong et al, *A Study on plasma edge boundary in ergodic layer of LHD based on radial profile measurement of impurity line emissions*, *Physics of Plasmas*, Vol.18 (2011), 082511, doi:10.1063/1.3626540.
- 2) Chunfeng Dong et al, *Study on Radial Position of Impurity Ions in Core and Edge Plasma of LHD Using Space-Resolved EUV Spectrometer*, *Plasma Science and Technology*, Vol.13, No.2 (April 2011), pp.140, doi:10.1088/1009-0630/13/2/03.
- 3) Chunfeng Dong et al, *Space-resolved extreme ultraviolet spectrometer for impurity emission profile measurement in Large Helical Device*, *Review of Scientific Instruments*, Vol. 81 (2010) 033107, doi:10.1063/1.3299060.

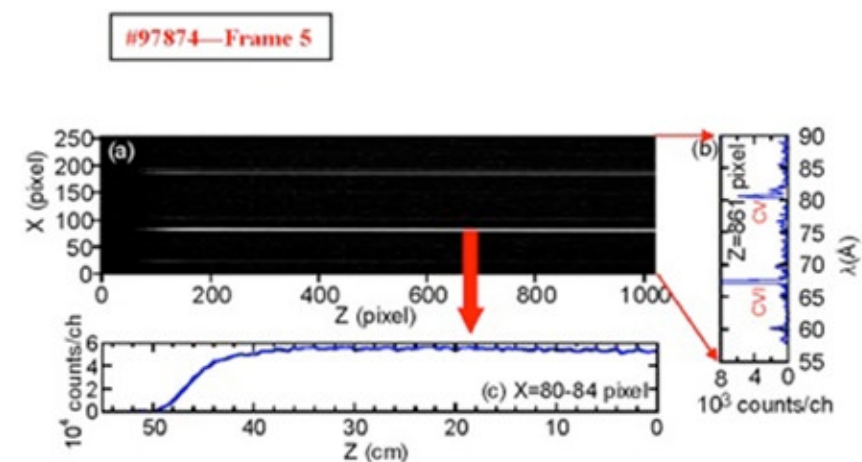


Fig. 1. This example of a space-resolved EUV line image was taken from EUV spectrometer with a back-illuminated CCD. The horizontal axis (Z) and vertical axis (X) denote the vertical position of LHD plasma and wavelength, respectively. Spectrum is indicated in right-hand inset, which is taken at Z=#861 pixel, and the vertical profile of Carbon 6 (C VI) (2nd order: $2 \times 33 \text{ \AA}$) is shown in bottom-side inset, which is taken at X=#80-84 pixels.

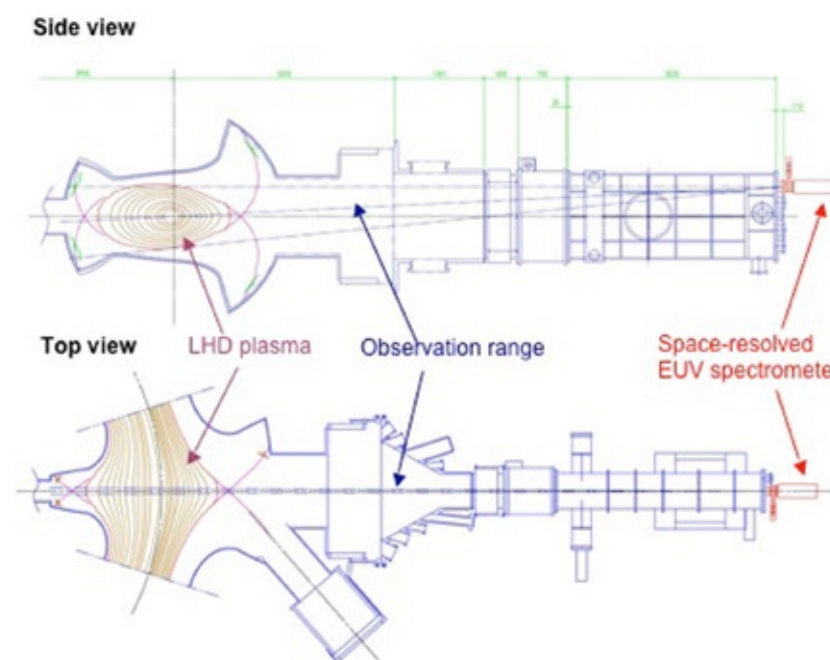


Fig. 2. Schematic drawings of space-resolved EUV spectrometer installed on LHD in side view and top view. The magnetic surface structure of the LHD at R=3.75 m plasma axis position shown on the left.

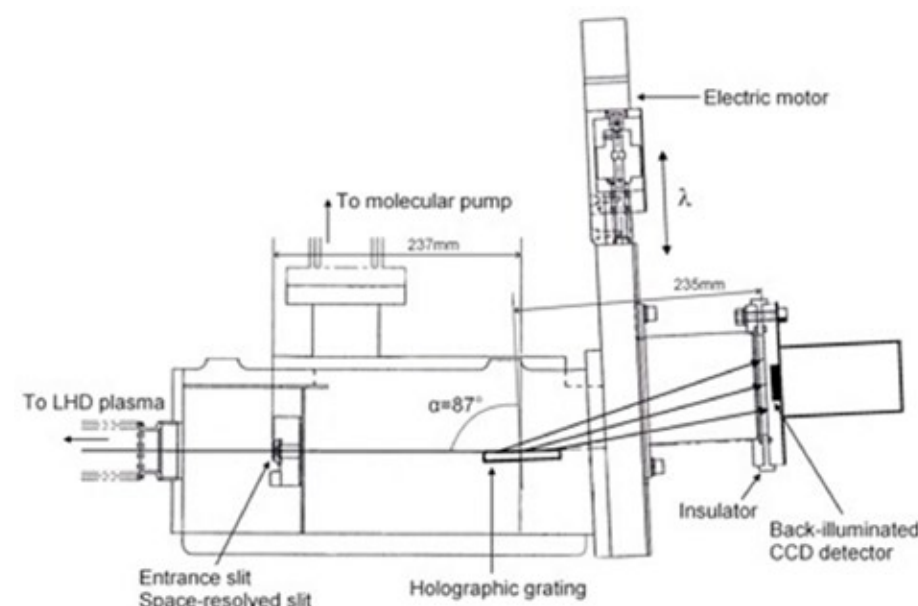


Fig. 3. Space-resolved EUV spectrometer installed on LHD. Spatial resolution in vertical direction is adjusted by a space-resolved slit. A wavelength range of 60 to 400 Angstroms can be observed by moving the CCD detector. It should be noted that the wavelength range has been expanded to 30 to 650 \AA after modifying the scanning system of the CCD.

Application Note

Neutron Radiography / Tomography

Why Image Neutrons?

Neutron imaging has wide industrial and scientific significance and can provide detailed information concerning the inner structure and composition of objects.

The principle of neutron imaging is based on the attenuation, through both scattering and absorption, of a directional neutron beam by the matter through which it passes. Since different materials vary in their ability to attenuate neutrons both composition and structure can be probed. The neutron beam can be generated either in a reactor, from a neutron emitting isotope, or from a target in a proton accelerator. The technique is also non-destructive in nature, and has been effectively applied to artefacts of archaeological significance.

The neutron imaging technique, rather than being in competition with X-Ray imaging, is entirely and ideally complimentary to it. Whereas X-Rays are scattered and absorbed by the electrons, and as such atoms with greater electron shells interact more strongly, neutrons on the other hand interact with the atomic nuclei. Furthermore, there is no real periodic regularity dictating the degree of this interaction, and even isotopes of the same element may differ markedly in their attenuation ability.

Of particular practical significance is the high contrast between hydrogen, which interacts very strongly with neutrons, and most metals, which offer effective transmission of neutrons. This is directly opposed to X-Ray imaging, and offers the means to effectively visualize the dynamics of organic hydrogen-containing substances in metal containers, such as the ability to visualize fuel within engines. It can also equally be used to view plastic seals or lubricants embedded within metal structures. The degree of attenuation for some materials can depend on the neutron energy, fast or thermal neutrons, such is the case with iron.

Neutron Imaging Technique

Neutron Radiography involves placing an object in the path of the neutron beam, and measuring the shadow image of the object that is projected onto a neutron detector. This often consists of a scintillator optically coupled to a CCD, sCMOS or EMCCD camera. Neutron Tomography takes this a step further and entails rotating the sample in the beam and recording multiple 2D images through an angular range of 180°. From the data set, a 3D representation through the object can be constructed. Fig. 1 shows a typical system setup.

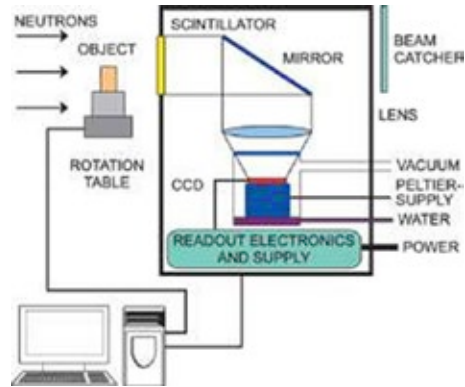


Fig. 1. Neutron Tomography schematic diagram

Camera Solutions for Neutron Radiography / Tomography

Traditionally CCD's have been used as imaging cameras for neutron tomography. Andor's scientific range of imaging cameras are ideal with their extremely low noise, -100 °C cooling and highest QE delivering optimal performance.

However, a limitation of CCD's for some neutron detection applications, such as dynamic processes in real time, can be the effective readout speed of 3-5 MHz. Although this is still extremely effective for monitoring stationary objects or slow processes, due to the features mentioned previously.

For the faster framing requirements, or to perform faster 3D tomography (or 4D (3D + time)), a different approach to the camera selection needs to be taken.

The Neo sCMOS is one such camera selection that delivers low noise, target field of view and 100 full frames per second rates faster for smaller regions of interest. If the application also requires single photon sensitivity then an EMCCD detector should be selected.

EMCCD detectors offer > 90% QE, as well as single photon sensitivity at frame rates of > 30 full frames / sec. EMCCD-enhanced sensitivity and speed opens the door on the ability to follow faster 3D tomography. The EMCCD gained overcomes the inherent optical losses of the system.

The QE curves in Fig. 2 and the cameras listed in Table 1 show some of the options available for Neutron Tomography.

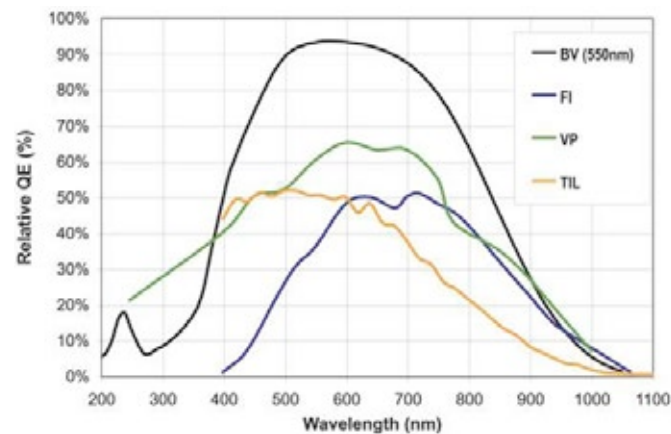


Fig. 2. A selection of QE curves

| | EMCCD | | | sCMOS | CCD | |
|-------------------------------|-----------------|-----------------|-----------------|------------------------|-------------------------------|----------------|
| | 860 | 897 | 888 | Neo | iKon L 936 | iKon M 934 |
| Active pixel (HxV) | 128 x 128 | 512 x 512 | 1024 x 1024 | 2560 x 2160 | 2048 x 2048 | 1024 x 1024 |
| Pixel size (µm ²) | 24 | 16 | 13 | 6.5 | 13.5 | 13 |
| Full frame rate | 515 | 35 | 8.9 | 100 | 0.92 | 2.2 |
| Read noise (e ⁻) | <1 with EM Gain | <1 with EM Gain | <1 with EM Gain | 1 Rolling Shutter Mode | 14 @ 3 MHz High Capacity Mode | 10.3 @ 2.5 MHz |
| Digitization | 14 and 16 bit | 14 and 16 bit | 14 and 16 bit | 16 bit | 16 bit | 16 bit |

Table 1. Key parameters for camera options for Neutron Tomography

Case Studies

Non-Destructive Testing (NDT)

Fig. 3 shows a virtual slice through a famous bronze sculpture "Mercure from Thalwil", exhibit of the Swiss National Museum, Zurich, Switzerland. With the help of Neutron Tomography it becomes possible to study inner structure and casting failures completely non-destructively. Neutrons are required because the commonly used X-Ray cannot penetrate the alloy, which contains high amounts of lead.

Neutron Tomography at NEUTRA facility, Paul Scherrer Institut, Switzerland. Images kindly supplied by Eberhard H. Lehmann of the NEUTRA facility.



Fig. 3 - Mercure from Thalwil

Investigating Organic Material

Fig. 5 shows a crab with an outer size of 20 cm, which was investigated to see the inner organs within the shell. Neutrons have high contrast for organic materials.

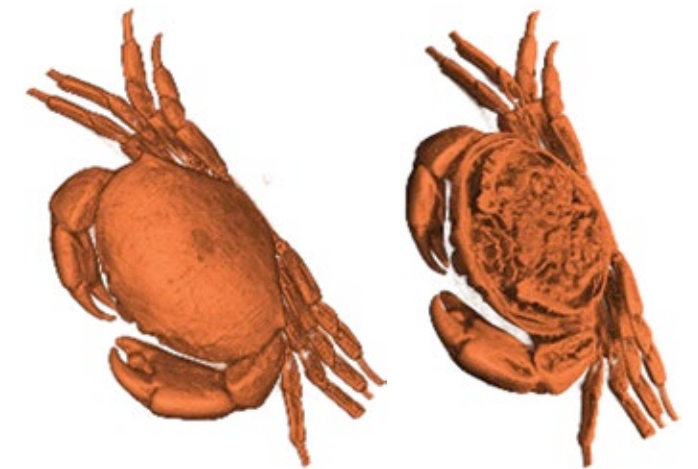


Fig. 5 - A crab showing the inner organs within the shell

In-situ Testing

Fig. 4 shows a sprinkler nozzle, which contains a tube filled with liquid. The sealing rings around it were inspected in-situ (as installed) for quality assurance and a functionality check. Rubber and liquids deliver high contrast for neutrons compared to the metallic structure around.

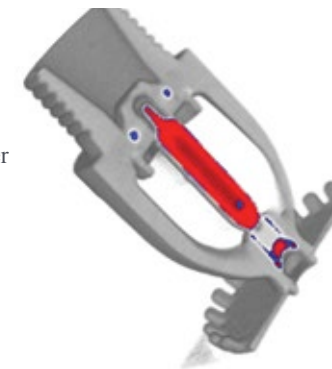


Fig. 4 - Cross section through a sprinkler nozzle.

Technical Note

Binning

CCD's are very versatile devices and their readout pattern can be manipulated to achieve various effects. One of the most commonly used is binning. Binning allows charges from adjacent pixels to be combined on the sensor before the charge is readout through the amplifier, the dominant noise source on a CCD. This can offer benefits in faster readout speeds and improved signal to noise ratios with reduced spatial resolution.

To illustrate the difference between the two readout modes we have used a step by step readout diagram.

The diagram is of a CCD made up of 4 pixel imaging array, in grey, with a readout register below, in blue. The charge held in the pixel is indicated in the bottom right of the pixel.

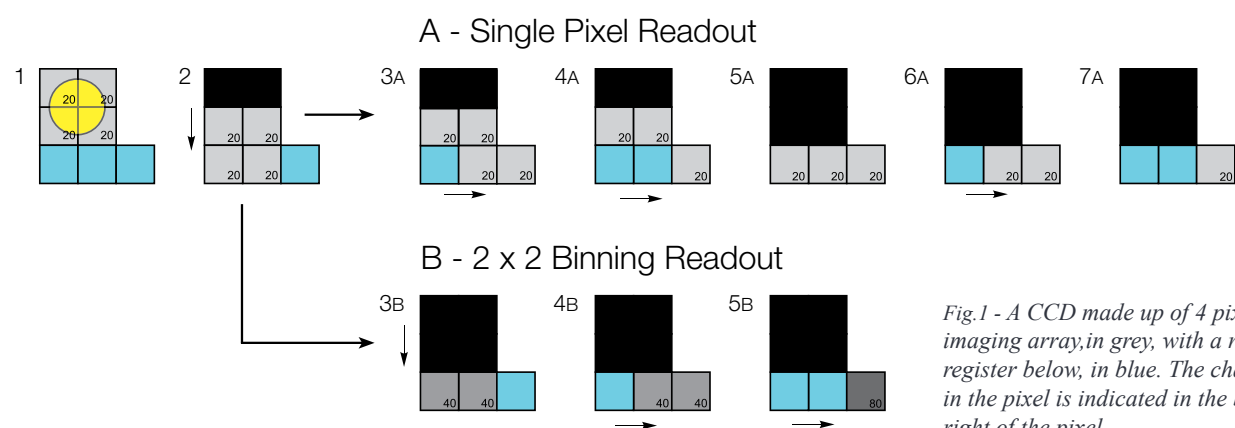


Fig.1 - A CCD made up of 4 pixel imaging array, in grey, with a readout register below, in blue. The charge held in the pixel is indicated in the bottom right of the pixel.

1. The light falls evenly on the four pixels and creates a charge of $20 e^-$ in each of the four pixels.
2. The first operation is to shift the charge down one row. The charge from the lowest pixels gets shifted into the readout register.
3. (A) For single pixel readout, the charge in the readout register is shifted to the right and into the readout amplifier. (B) In the binning operation the charge is shifted down again and the charge from the first row is added, or summed, to the first row in the readout register.
4. (A) For single pixel readout, the first pixel is readout while the readout register is shifted again to shift the charge in the second pixel into the readout amplifier. (B) In the binning operation the summed charge from two right two pixels is shifted into the readout amplifier.
5. (A) In the single pixel readout, the next row is shifted vertically into the readout register. (B) In the binning operation the readout register is shifted again to sum the charge from the five pixels in the readout amplifier before being readout.
6. (A) In the single pixel readout mode, the readout register is shifted to the right again to readout the next pixel. Binned operation is now complete.
7. (A) In the single pixel readout the readout register is shifted to the right again to readout the final pixel.

It is important to highlight the main differences in the two readout schemes. In the first we achieve the full spatial resolution of the sensors array. In the binned example we have reduced the 4 pixel pattern to a single pixel 'Superpixel' and hence have lost spatial resolution. However, the binned operation takes fewer steps to readout the sensor and hence is faster. Typically binning 2×2 is twice as fast; this is achieved by having to shift the readout register only every two vertical shifts. This relationship holds if we were binning 3×3 or 4×4 on a CCD with the readout being three and four times faster respectively.

The binned example also highlights how binning improves the signal to noise ratio. If we assume our CCD has a readout noise of $10 e^-$, then in the single pixel example each pixel is readout with a noise of $10 e^-$ hence we achieve a signal to noise ratio of 2:1 ($20 e^- / 10 e^-$). Even if we subsequently sum the four pixels in a computer after readout the signal to noise ratio becomes 4:1. In summing the charge of the four pixels, we sum the signal ($4 \times 20 e^-$ i.e. $80 e^-$) and the noise is added in quadrature i.e. square root of the sum of the noises squared ($\sqrt{4 \times (10 e^-)^2}$ i.e. $20 e^-$).

In the binned example there is no noise until the signal is readout by the amplifier, so the signal to noise ratio is 8:1 ($80 e^- / 10 e^-$) i.e. twice as good as the single pixel readout mode.

One of the most common applications of custom binning in X-Ray is in energy-dispersive spectroscopy where low flux conditions with incident higher energies X-Ray photons can be directly detected with the larger superpixel gaining the advantage of the lower noise and faster readout to achieve a user definable optimal performance.

Technical Note

Cropped Mode

If an experiment demands fast temporal resolution, but requires a sequence of images greater than the maximum storage available with the on-chip array, then it is possible to readout Andor camera families in a special user-selectable 'cropped mode'.

In this mode, the user defines a 'sub-array' size from within the full image sensor area, such that it totally encompasses the region of the image where the sensor is illuminated by the signal of interest (e.g. a 'beam spot'). The camera will subsequently process the sensor array of this smaller user defined array size. This is achieved through the firmware/software executing special readout patterns and this benefits the user because the readout is at a proportionally faster frame rate. The smaller the defined array size, the faster the frame rate achievable. The selected region should be placed in the area adjoining the shift register, therefore close to the readout amplifier, to achieve the fastest repetition rate. Full and cropped image mode shown in Fig. 1 and 2.

In order to use cropped mode effectively, one has to ensure that no light is falling on the light sensitive area outside of the user defined region. This is because any light collected outside the cropped area will be clocked through the region of interest thereby corrupting the desired images being acquired in this mode. Cropped mode has the end result of achieving a much faster frame rate than that obtainable in a conventional 'sub-array' / ROI readout (during which we would still have to vertically shift the unwanted rows) as the frame rate increase is achieved by not reading out (i.e. discarding) the unwanted pixels.

Cropped Mode

The active imaging area of the sensor is user defined with a small sub section of the entire chip used for the actual imaging. The remaining array has to be masked to prevent stray light leakage or charge blooming from this region. This would compromise the signal from the defined imaging area. By cropping the sensor one achieves faster frame rates because the temporal resolution will be dictated by the time that is required to read out, the now smaller section of the sensor.

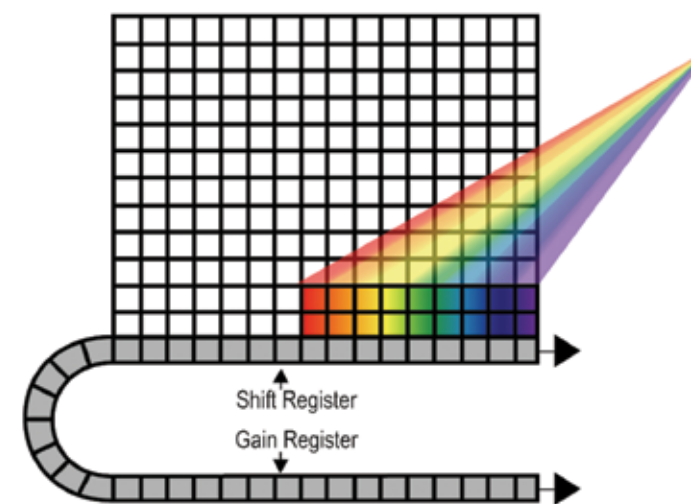


Fig. 1. Full EM Sensor



Fig. 2. 'Cropped' EM Sensor

Technical Note

Quantum Efficiency (QE)

The QE of the CCD is governed by the ability of the incident photons to be absorbed in the depletion region of the sensor. To understand how the photon is absorbed in this key region, or not, is a key factor in understanding the QE range of the variety of sensors on offer. Although there are other factors which effect the final shape of the QE curve such as the different materials and their different absorption coefficient and the reflectance of the silicon the most dominant and straightforward impact on the sensor QE is the structure of the actual CCD. If we look at the CCD in cross-section it helps to illustrate this point as shown in Fig. 1.

In a front illuminated device, photons falling on the CCD must travel through the region of the gate electrodes structures. These structures are very strong absorbers of lower energy X-Ray photons, which can be absorbed within a few nm of material.

As a general rule, the absorption length of the incident X-Ray increases, that is lengthens, with increasing energy. If we apply this simple rule to photons incident on the CCD structure, we can see that in a front illuminated device photons must travel through the regions of the gate electrodes structures, AR coating (if applicable) and the oxide layer, effectively making up a 'dead zone' before entering the depletion zone. The effective depth of this zone will also delineate the probability of absorption of the higher energy photons, with the incident photons energies increasing to a point where their absorption length is longer than the depth, hence the probability of capture approaches zero. This also explains the QE strengthening to a peak then reducing as the energy increases. Another point to note is that the discontinuities or edges seen in the QE are the result of the intrinsic properties of the silicon, the absorption edges L-edge at 100.6 eV and K-edge at 1.8 keV.

Other Sensors:-

Deep Depletion sensors, as the name suggests, extend the depth of the depletion zone and thereby increase the higher energy range that they can directly detect.

Back-illuminated sensors are sensors that have been effectively inverted so the electrode structure is no longer on the top surface but the bottom. The bulk of silicon is also removed leaving only a very thin 'dead zone' layer, thus allowing the softer X-Ray detection.

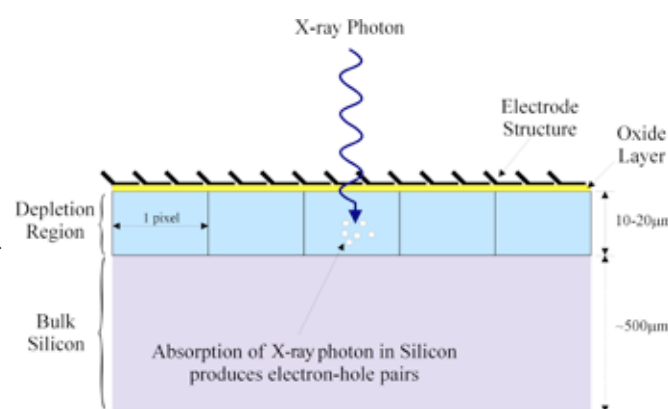


Fig. 1. A schematic cross-section illustrating direct detection of an X-Ray photon by a CCD sensor.

Technical Note

Indirect Detection

With energies of >22 keV, the CCD is no longer able to directly detect the incident photons. This means a transducer needs to be introduced into the system to convert the incident photons to photons, which are again visible to the detector.

'Two Step' Detection

The first step in this 'two step' detection is a material, commonly a scintillator, to convert the incident X-Ray's photons into visible wavelength photons, which can then be directly detected by the CCD in the second step. These 'converter' materials comprise of an extensive range of options of both phosphors and scintillators, selection depends on the specific requirement for detection, for example energy range, spatial resolution etc.

As is shown in the sensor range diagram, this method of detection is the only option once the energies of X-Ray photons (>20 keV) are to be detected as the CCD is no longer able to absorb the photons within the depletion zone. The requirement to convert the incident photon has some key disadvantages, primarily the actual conversion process is very inefficient. Also, as the incident photon is no longer directly detected there is no longer the ability to correlate the number of electrons to the incident energies. There has been a series of evolutions of design and in the components, which has improved the detection of signal.

Methods of Indirect Detection

Phosphor

The sensor is coated with a phosphor, for example Gadolinium Oxysulphide ($Gd_2O_3:S:Tb$) often referred to as GADOX, also known as P43. This phosphor absorbs X-Ray photons and emits visible photons predominately at 545 nm (2.28 eV), and has approximately a 15% conversion efficiency, i.e. 15% of the absorbed X-Ray photon energy is converted into visible photons. However, only a fraction of these generated photons will reach the detector as they are emitted in all directions. This illustrates the inefficiency of the conversion process with both signal and spatial resolution, as the secondary emission will effectively spread from the generation point. Increasing the depth of the scintillator, or phosphor, relates to the energy range that it will be able to absorb and convert, however the thicker it becomes, there is an equivalent reduction in the spatial resolution, so again a balance must be found.

Fiber Faceplate and Scintillator/Phosphor

The next development was to place fiber-optic, coated or bonded to a scintillator. This effectively acts to maintain spatial resolution as it channels the light via the individual fibers onto the sensor, reducing the spread of the light from the generation point. The introduction of the fiber-optic has other important advantages, the fiber can be extruded to form a taper, this increases the area that can be imaged, albeit with a demagnification of the image. It can also offer protection to the sensor from the harder X-Rays, which are in themselves damaging to the silicon structure of the CCD.

Lens Based Systems

There has been a growing interest in the use of lens-based camera systems to image scintillator screens. The method is popular as the active area of the scintillator can be very large, 50 cm² and larger. With the camera protected from the direct path of the damaging hard X-Ray, even neutron and gamma sources can be used in this method. From a camera position this is also a simpler and easier method as there is no need to modify or change the standard camera which allows for a quick and easy replacement or upgrade.

Each of these versions have their associated advantages and disadvantages, however some simple rules can be applied:

- The more components in the optical path the less the transmission
- Higher Spatial resolution requires the light to be channelled or focussed
- If imaging greater than 5x sensor area a lens system is required
- If the distance from scintillator >10 's cm, a lens is required

There are further variations on these basic types of indirect detection. At Andor we have cameras in all versions and we use a dedicated team to design and build these bespoke systems. The design process looks at the requirements and matches the variety of components options, such as fiber and scintillator, to produce a final quality Andor product. Contact your local sales representative. For details of our CSR (Customer Special Request) process, see page 20 where we can deliver an Andor quality camera for your specific requirement.

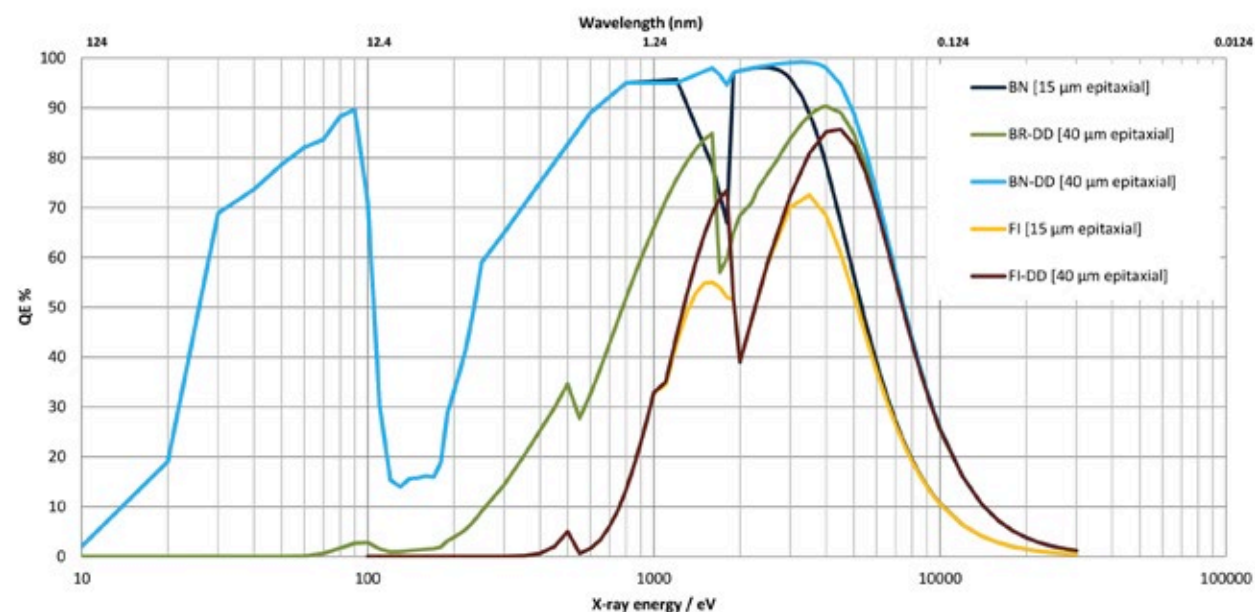


Fig. 2. Quantum efficiency curves for a range of sensor types - direct detection

Technical Note

Direct Detection

Direct detection occurs when an incident photon is absorbed within the silicon of the CCD, resulting in the production of the electron-hole (e-h) pairs. If this absorption occurs within the depletion region of the CCD, the electrons and holes are separated by the applied internal electric field, generated by the CCD's electrode structure. The electrons are being trapped by the field and the holes undergo rapid recombination. The trapped electrons can subsequently be 'clocked' to the amplifier and readout. For this reason only the electrons of the e-h pairs formed in the depletion zone will be read out as signal. When an incident photon is absorbed, the number of e-h pairs formed and the size of the cloud they form in the silicon is directly related to the energy of the incident photon. These relationships are shown in the graphs and tables that follow.

The equation holds for photon energies >10 eV, assuming an ideal quantum yield.

$$N_{e-h} = \frac{E(eV)}{E_{e-h}} \quad \text{e.g. For } 5.9 \text{ keV } \quad N_{e-h} = \frac{5900}{3.65} = 1616 e^-$$

N_{e-h} - Average number of e-h pairs formed
 E_{e-h} - Energy required to generate an e-h pair 3.65 eV/e⁻ for Silicon at RT
 $E(eV)$ - Energy of the incident photon

Energy-Dispersion Detection

The relationship between incident photon energy and the number of electrons that are generated in the CCD means that in a low flux situation, single photons per pixel events, the energy of the X-Ray source can be calculated. This powerful technique is key for EDS [energy-dispersive spectroscopic] applications. This is possible by using the histogram generated from the image pixels signal levels. The peaks found in this histogram give a count level from which the number of electrons generated can be derived using the cameras sensitivity, the incident photon energy can then be found.

Energy Resolution

The energy resolution is a measure of the ability to resolve individual energy lines. It can be calculated by the FWHM of the energy peaks. The theoretical limiting energy resolution for a CCD is related by the equation* below.

$$FWHM(eV) = 2.355[E(eV)E_{e-h} F_a]^{1/2}$$

F_a = Fano Factor = 0.1*
 $E(eV)$ = Energy of incident photon
 E_{e-h} = energy to generate a e-h pair

| Unit Conversion | |
|-----------------|---------------------|
| Wavelength | Pressure |
| 1 nm = 10 Å | 1 Torr = 1/760 atm |
| eV = 1239 / nm | 1 Torr = 133.322 Pa |
| | 1 Torr ≈ 1 mbar |

The direct detection energy resolution of a CCD camera is an effective method of testing the performance of the camera. The design and interface must be optimal to approach the theoretical energy resolution, with all the cameras key performance parameters optimised.

Andor builds the worlds leading cameras because we optimise these parameters to achieve the best system performance, from the design through to the final build stage of our world leading camera platforms. Across the system's key parameters the highest performance must be achieved; charged transfer efficiency [CTE], the noise of the electronics, the lowest dark current a linear response over the entire dynamic range, at Andor we do this as standard.

| Energy Range (eV) | e-h pairs generated per absorbed photon |
|-------------------|---|
| 1.1-3.1 | single e-h pair |
| >3.1 | multiple e-h pairs |

Table 1. Relationship of electron whole generation to energy range

*The Fano Factor is an empirical constant used to determine the variation in charge generated when an X-Ray photon or particles interact. The factor is empirically derived and is determined to be 0.1.

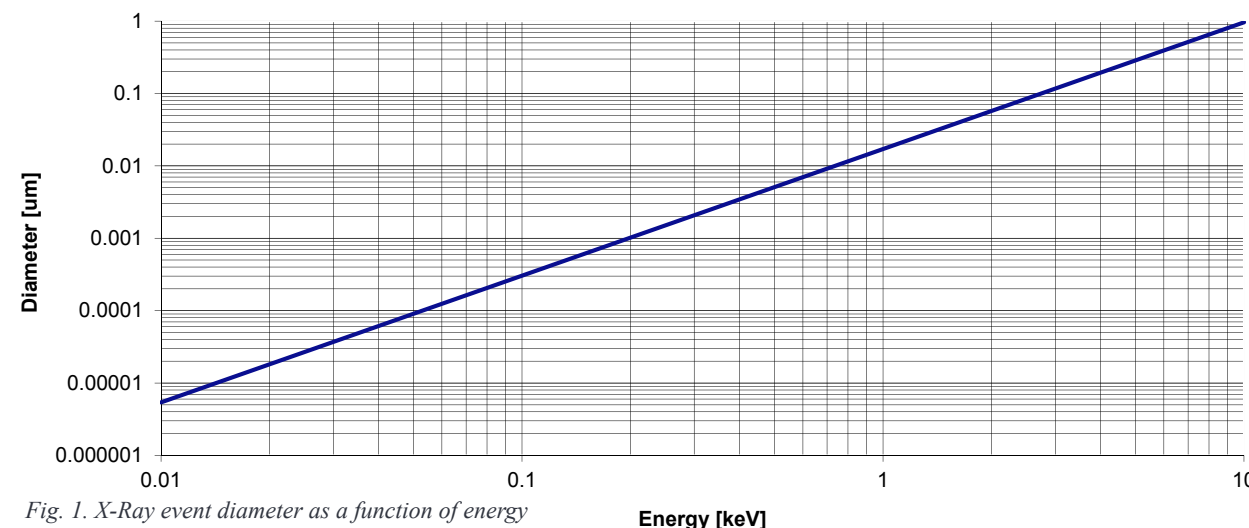


Fig. 1. X-Ray event diameter as a function of energy

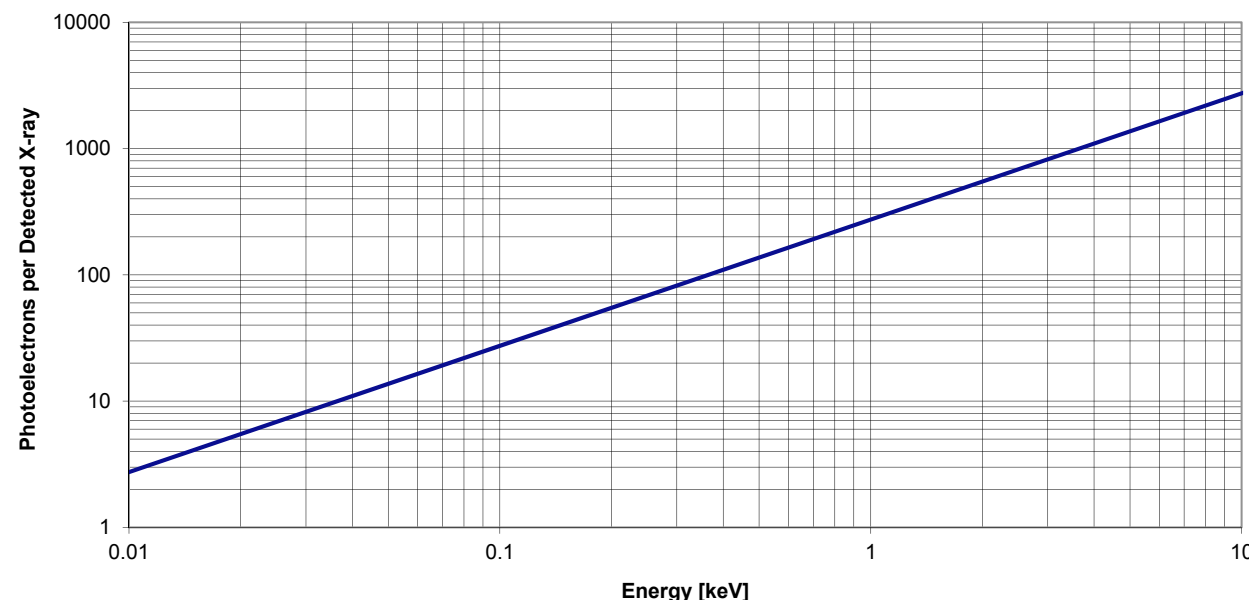


Fig. 2. Relationship between incident X-Ray and number of photoelectrons generated

| X-Ray photon energy (keV) | Wavelength (nm) | Wavelength (Å) | e-h pairs generated per detected X-Ray | Diameter of electron cloud (µm) | Calibration Source |
|---------------------------|-----------------|----------------|--|---------------------------------|---------------------------------|
| 0.01 | 124.00 | 1240 | 3 | 0.00001 | |
| 0.1 | 12.40 | 124 | 27 | 0.00030 | |
| 0.5 | 2.48 | 24.8 | 137 | 0.00508 | |
| 1 | 1.24 | 12.4 | 274 | 0.01710 | |
| 5 | 0.25 | 2.48 | 1370 | 0.28589 | |
| 5.9 | 0.21 | 2.1 | 1616 | 0.38193 | Fe ⁵⁵ K _α |
| 10 | 0.12 | 1.24 | 2740 | 0.96160 | |
| 11 | 0.11 | 1.13 | 3014 | 1.13614 | |

Table 2. Table of key parameters

Standard Part Numbers

Cameras

Zyla HF

| | |
|--------------|--|
| ZYLA5.5X-FO | sCMOS, 2560 x 2160 (5.5 MP), 6.5 µm, FI, 100 fps, global & rolling shutter, FOP |
| ZYLA5.5X-FOR | sCMOS, 2560 x 2160 (5.5 MP), 6.5 µm, FI, 100 fps, global & rolling shutter, FOP, high resolution scintillator fitted |

Newton SO

| | |
|--------------|--|
| DO920P-FI | CCD, 1024 x 256, 26 µm, FI, No AR coating, AIMO, 3MHz |
| DO920P-BN | CCD, 1024 x 256, 26 µm, BI, No AR Coating, AIMO, 3 MHz |
| DO920P-BR-DD | CCD, 1024 x 256, 26 µm, Deep Depletion, BI, NIR Coating, NIMO, 3 MHz |

iKon-L SO

| | |
|----------------|---|
| DO936N-M0W-#FI | CCD, 2048 x 2048, 13.5 µm, FI, No AR Coating, AIMO, 5 MHz |
| DO936N-M0W-#BN | CCD, 2048 x 2048, 13.5 µm, BI, No AR Coating, AIMO, 5 MHz |
| DO936N-M0W-BRD | CCD, 2048 x 2048, 13.5 µm, Deep Depletion, BI, NIR coating, NIMO, 5 MHz |
| DO936N-M0Z-#FI | CCD, 2048 x 2048, 13.5 µm, FI, No AR Coating, AIMO, 5 MHz |
| DO936N-M0Z-#BN | CCD, 2048 x 2048, 13.5 µm, BI, No AR Coating, AIMO, 5 MHz |
| DO936N-M0Z-BRD | CCD, 2048 x 2048, 13.5 µm, Deep Depletion, BI, NIR coating, NIMO, 5 MHz |
| DO936N-I0W-#FI | CCD, 2048 x 2048, 13.5 µm, FI, No AR Coating, AIMO, 5 MHz |
| DO936N-I0W-#BN | CCD, 2048 x 2048, 13.5 µm, BI, No AR Coating, AIMO, 5 MHz |
| DO936N-I0W-BRD | CCD, 2048 x 2048, 13.5 µm, Deep Depletion, BI, NIR coating, NIMO, 5 MHz |

iKon-M SO

| | |
|--------------|--|
| DO934P-BN | CCD, 1024 x 1024, 13 µm, BI No AR coating, AIMO, 5 MHz |
| DO934P-BR-DD | CCD, 1024 x 1024, Deep Depletion, BI-DD, NIR AR Coating, NIMO, 5 MHz |
| DO934P-FI | CCD, 1024 x 1024, 13 µm, FI, No AR Coating, AIMO, 5 MHz |

| | |
|--------------|--|
| ZYLA5.5X-FOT | sCMOS, 2560 x 2160 (5.5 MP), 6.5 µm, FI, 100 fps, global & rolling shutter, FOP, high throughput scintillator fitted |
|--------------|--|

| | |
|-----------|--|
| DO940P-FI | CCD, 2048 x 512, 13.5 µm, FI, No AR Coating, AIMO, 3 MHz |
| DO940P-BN | CCD, 2048 x 512, 13.5 µm, BI, No AR Coating, AIMO, 3 MHz |

| | |
|----------------|---|
| DO936N-I0Z-#FI | CCD, 2048 x 2048, 13.5 µm, FI, No AR Coating, AIMO, 5 MHz |
| DO936N-I0Z-#BN | CCD, 2048 x 2048, 13.5 µm, BI, No AR Coating, AIMO, 5 MHz |
| DO936N-I0Z-BRD | CCD, 2048 x 2048, 13.5 µm, Deep Depletion, BI, NIR coating, NIMO, 5 MHz |
| DO936N-O0W-#FI | CCD, 2048 x 2048, 13.5 µm, FI, No AR Coating, AIMO, 5 MHz |
| DO936N-O0W-#BN | CCD, 2048 x 2048, 13.5 µm, BI, No AR Coating, AIMO, 5 MHz |
| DO936N-O0W-BRD | CCD, 2048 x 2048, 13.5 µm, Deep Depletion, BI, NIR coating, NIMO, 5 MHz |
| DO936N-O0Z-#FI | CCD, 2048 x 2048, 13.5 µm, FI, No AR Coating, AIMO, 5 MHz |
| DO936N-O0Z-#BN | CCD, 2048 x 2048, 13.5 µm, BI, No AR Coating, AIMO, 5 MHz |
| DO936N-O0Z-BRD | CCD, 2048 x 2048, 13.5 µm, Deep Depletion, BI, NIR coating, NIMO, 5 MHz |

iKon-M SY

| | |
|--------------|---|
| DY934P-FI | CCD, 1024 x 1024, 13 µm, FI, No AR Coating, AIMO, 5 MHz, Be Foil |
| DY934P-BN | CCD, 1024 x 1024, 13 µm, BI No AR coating, AIMO, 5 MHz, Be Foil |
| DY934P-BR-DD | CCD, 1024 x 1024, Deep Depletion, BI-DD, NIR AR Coating, NIMO, 5 MHz, Be Foil |

Cameras cont.

Newton SY

| | |
|-----------------|--|
| DY920P-FI-T2 | CCD, 1024 x 256, 26 µm, FI, No AR coating, AIMO, 3 MHz, Be Foil |
| DY920P-FI-DD-T2 | CCD, 1024 x 256, 26 µm, Deep Depletion, FI-DD, No AR Coating, NIMO, 3 MHz, Be Foil |
| DY920P-BN-T2 | CCD, 1024 x 256, 26 µm, BI, No AR Coating, AIMO, 3 MHz, Be Foil |

iKon-L SY

| | |
|--------------|--|
| DY936N-BN | CCD, 2048 x 2048, 13.5 µm, BI, No AR Coating, AIMO, 5 MHz, Be Foil |
| DY936N-BR-DD | CCD, 2048 x 2048, 13.5 µm, Deep Depletion, BI, NIR coating, NIMO, 5 MHz, Be Foil |

iXon HF

| | |
|----------|---|
| DF897-FB | CCD, 512 x 512FT, 16 µm, EMCCD, BI, Mid Band, AR Coating, AIMO, 10 MHz, FOP |
|----------|---|

| | |
|-----------------|---|
| DY920P-BR-DD-T2 | CCD, 1024 x 256, 26 µm, Deep Depletion, BI, NIR Coating, NIMO, 3 MHz, Be Foil |
| DY940P-FI-T2 | CCD, 2048 x 512, 13.5 µm, FI, No AR Coating, AIMO, 3 MHz, Be Foil |
| DY940P-BN-T2 | CCD, 2048 x 512, 13.5 µm, BI, No AR Coating, AIMO, 3 MHz, Be Foil |

iKon-L HF

| | |
|-----------------|---|
| DF936N-FB-T2 | CCD, 2048 x 2048, 13.5 µm, BI, Mid Band AR coating, AIMO, 5 MHz, FOP |
| DF936N-FB-HR-T2 | CCD, 2048 x 2048, 13.5 µm, BI, Mid Band AR coating, AIMO, 5 MHz, FOP with High Resolution scintillator fitted |
| DF936N-FB-HT-T2 | CCD, 2048 x 2048, 13.5 µm, BI, Mid Band AR coating, AIMO, 5 MHz, FOP with High Throughput scintillator fitted |

Accessories

| | |
|------------------|--|
| ACC-MEC-08444 | Zyla HF filter holder |
| ACC-MEC-05764 | O-Y converter flange with Be window 250 µm and KF fitting for pump |
| ACC-MEC-07873 | Filter & scintillator holder |
| ACC-MEC-08169 | 1:1.9 Taper Module |
| ACC-OPT-07875 | Be foil, Ø56 mm, 200 µm thick |
| XW-RECR | Re-circulator for enhanced cooling performance |
| ACC-XW-CHIL-160 | Oasis 160 ultra compact chiller unit |
| XU-RECR/TRANS | USB 2.0 - transmitter and receiver. Including 2 power supplies |
| XF-FILTER HOLDER | Optional filter holder for iKon-L ['O' interface] |

Have you found what you're looking for?

If you need another combination of options not covered on these pages, please contact us for further information. For more challenging proposals why not use our CSR* Team.



Research Papers

| | |
|--|--|
| Neutron radiography and current distribution measurements for studying cathode flow field properties of direct methanol fuel cells | A. Schröder et al, International Journal of Energy Research, volume 38, issue 7, doi:10.1002/er.3094 (2014) |
| Quantitative tabletop coherent diffraction imaging microscope for EUV lithography mask inspection | Bosheng Zhang et al, SPIE Proceedings of the Metrology, Inspection, and Process Control for Microlithography XXVIII, doi:10.1117/12.2046526 (2014) |
| Time Resolved Holography Scheme using a Table top Soft X-ray Laser | E. Malm et al, Springer Proceedings in Physics, volume 147, doi: 10.1007/978-3-319-00696-3_26 (2014) |
| Ultrafast Imaging of Shocked Material Dynamics with X-ray Free Electron Laser Pulses | Richard Sandberg et al, proceedings of CLEO: Science and Innovations (2014) |
| X-ray detection capability of a Cs2ZnCl4 single-crystal scintillator | Natsuna Yahaba et al, Applied Physics Express, volume 7, issue 6 (2014), doi:10.7567/APEX.7.062602 |
| Coded Aperture Imaging for Fluorescent X-rays-Biomedical Applications | A. Haboub et al, proceedings of the Fully Three-Dimensional Image Reconstruction in Radiology and Nuclear Medicine (2013) |
| Coherent synchrotron emission in transmission from ultrathin relativistic laser plasmas | B. Dromey et al, New Journal of Physics, volume 15, doi: 10.1088/1367-2630/15/1/015025 (2013) |
| Hanbury Brown–Twiss Interferometry at a Free-Electron Laser | A. Singer et al, Physical Review Letters, volume 111, doi: 10.1103/PhysRevLett.111.034802 (2013) |
| In situ coherent X-ray diffraction of isolated core–shell nanowires | Sabine T. Haag et al, Thin solid films, volume 530, doi: 10.1016/j.tsf.2012.07.060 (2013) |
| Interaction of magnetic nanoparticles with U87MG cells studied by synchrotron radiation X-ray fluorescence techniques | A. Gianoncelli et al, X-Ray Spectrometry, volume 42, issue 4, doi:10.1002/xrs.2475 (2013) |
| L-Edge X-ray Absorption Spectroscopy of Dilute Systems Relevant to Metalloproteins Using an X-ray Free-Electron Laser | Rolf Mitzner et al, The Journal of Physical Chemistry Letters, volume 4, issue 21, doi: 10.1021/jz401837f (2013) |
| Optical control of hard X-ray polarization by electron injection in a laser wakefield accelerator | Michael Schnell et al, Nature Communications, volume 4, doi:10.1038/ncomms3421 (2013) |
| Single pulse coherence measurements in the water window at the free-electron laser FLASH | D. Mai et al, Optics Express, volume 21, issue 11, doi: 10.1364/OE.21.013005 (2013) |
| Spatially resolved analysis of Kα x-ray emission from plasmas induced by a femtosecond weakly relativistic laser pulse at various polarizations | G. Cristoforetti et al, Physical Review A, volume 87, doi: 10.1103/PhysRevA.87.023103 (2013) |
| Study of crystalline thin films and nanofibers by means of the laser–plasma EUV-source based microscopy | P.W. Wachulak et al, Radiation Physics and Chemistry, volume 93, doi: 10.1016/j.radphyschem.2013.02.019 (2013) |
| Sub 1-μm resolution “water-window” microscopy using a compact, laser-plasma SXR source based on a double stream gas-puff target | Przemyslaw Wachulak et al, Nuclear Instruments and Methods in Physics Research Section B: Beam Interactions with Materials and Atoms, volume 311, doi: 10.1016/j.nimb.2013.06.001 (2013) |
| Tabletop single-shot extreme ultraviolet Fourier transform holography of an extended object | Erik B. Malm et al, Optics Express, volume 21, issue 8, doi: 10.1364/OE.21.009959 (2013) |
| X-ray ptychography with highly-curved wavefront | S. Wang et al, Journal of Physics: Conference Series, volume 463, doi:10.1088/1742-6596/463/1/012040 (2013) |
| Bulk dislocation core dissociation probed by coherent X-rays in silicon | V. L. R. Jacques et al, Physical Review Letters, volume 106, issue 6, doi: 10.1103/PhysRevLett.106.065502 (2011) |

| | |
|---|--|
| Controlling the spacing of attosecond pulse trains from relativistic surface plasmas | M. Behmke et al, Physical Review Letters, volume 106, issue 18, doi: 10.1103/PhysRevLett.106.185002 (2011) |
| Cryo transmission X-ray imaging of the malaria parasite, <i>P. Falciparum</i> | Hanssen et al, Journal of Structural Biology, doi: 10.1016/j.jsb.2010.08.013 (2011) |
| Demonstration of soft X-ray laser of Ne-like Ar at 69.8 nm pumped by capillary discharge | Yongpeng Zhao et al, Optics Letters, volume 36, issue 17, doi: 10.1364/OL.36.003458 (2011) |
| Density diagnostic of highly ionized samarium laser produced plasma using Ni-like spatially resolved spectra | E. Louzon et al, Laser and Particle Beams, volume 29, issue 1, doi: 10.1017/S0263034610000765 (2011) |
| Differential energy measurement between He- and Li-like uranium intra-shell transitions | M. Trassinelli et al, Physica Scripta, volume 2011, issue T144, doi: 10.1088/0031-8949/2011/T144/014003 (2011) |
| Electron beam density study using a portable slit imaging system at the Shanghai Electron Beam Ion Trap | Yang Yang et al, Chinese Physics B, volume 20, issue 8, doi:10.1088/1674-1056/20/8/080701 (2011) |
| High-order harmonic generation directly from a filament | D. S. Steingrube et al, New Journal of Physics, volume 13, issue 40634, doi:10.1088/1367-2630/13/4/043022 (2011) |
| Observation of K-Shell soft X-ray emission of nitrogen irradiated by XUV-free electron laser FLASH at intensities greater than 1016 W/cm² | E. Galtier et al, Contributions to Plasma Physics, volume 51, issue 2-3, doi: 10.1002/ctpp.201000045 (2011) |
| Study of extreme ultraviolet and soft X-ray emission of metal targets produced by laser-plasma-interaction | I. Mantouvalou et al, Review of Scientific Instruments, volume 82, issue 6, doi: 10.1063/1.3600069 (2011) |
| (Time-Resolved) hydrino continuum transitions with cutoffs at 22.8 nm and 10.1 nm | R. L. Mills et al, International Journal of Hydrogen Energy, volume 35, issue 16, doi: 10.1140/epjd/e2011-20246-5 (2011) |
| X-ray micro-tomography-based non-destructive evaluation of microwelds in an HDR source assembly used for brachytherapy | P. S. Sarkar et al, Insight - Non-Destructive Testing and Condition Monitoring, volume 53, issue 1 (2011) |
| EUV diagnostics of pulsed plasma systems | Mohanty et al, Journal of Physics: Conference Series, volume 208, issue 1, doi:10.1088/1742-6596/208/1/012138 (2010) |
| Metallic plate corrosion and uptake of corrosion products by Nafion in polymer electrolyte membrane fuel cells | Bozzini et al, ChemSusChem, volume 3, issue 7, doi: 10.1002/cssc.201000048 (2010) |
| Shafranov shift measurements by a soft X-ray CCD camera for internal diffusion barrier discharges in the Large Helical Device | Suzuki et al, Nuclear Fusion, volume 50, issue 6, doi: 10.1088/0029-5515/50/6/064013 (2010) |
| Space-resolved vacuum UV spectrometer system for edge impurity and temperature profile measurement in HL-2A | Cui et al, Review of Scientific Instruments, volume 81, issue 4, doi: 10.1063/1.3378288 (2010) |
| Three-dimensional coherent X-ray diffractive imaging from a single view | Sandberg et al, proceedings of Lasers and Electro-Optics (CLEO) and Quantum Electronics and Laser Science Conference (QELS), doi: 10.1364/CLEO.2010.CPDB1 (2010) |
| X-ray flash radiography system for a high-current discharge in a dense gas | Pinchuk et al, Instruments and Experimental Techniques, volume 53, issue 5, doi: 10.1134/S0020441210050192 (2010) |

Customer Support

Andor products are regularly used in critical applications and we can provide a variety of customer support services to maximize the return on your investment and ensure that your product continues to operate at its optimum performance.

Andor has customer support teams located across North America, Asia and Europe, allowing us to provide local technical assistance and advice. Requests for support can be made at any time by contacting our technical support team at andor.com/support.

Andor offers a variety of support under the following format:

- On-site product specialists can assist you with the installation and commissioning of your chosen product
- Training services can be provided on-site or remotely via the Internet
- A testing service to confirm the integrity and optimize the performance of existing equipment in the field is also available on request.

A range of extended warranty packages are available for Andor products giving you the flexibility to choose one appropriate for your needs. These warranties allow you to obtain additional levels of service and include both on-site and remote support options, and may be purchased on a multi-year basis allowing users to fix their support costs over the operating life cycle of the products.



Head Office

7 Millennium Way
Springvale Business Park
Belfast BT12 7AL
Northern Ireland
Tel: +44 (0)28 9023 7126
Fax: +44 (0)28 9031 0792

North America

425 Sullivan Avenue
Suite 3
South Windsor, CT 06074
USA
Tel: +1 860-290-9211
Fax: +1 860-290-9566

Japan

4F TK Sarugakucho Building
2-7-6 Sarugaku-Cho
Chiyoda-Ku
Tokyo 101-0064
Japan
Tel: +81 (0)3-3518-6488
Fax: +81 (0)3-3518-6489

China

Room 1213, Building B
Luo Ke Time Square
No. 103 Huizhongli
Chaoyang District
Beijing 100101
China
Tel: +86 (0)10-5129-4977
Fax: +86 (0)10-6445-5401

Find us on

